11-year record of wintertime snow surface energy balance and sublimation at 4863 m a.s.l. on Chhota Shigri Glacier moraine (western Himalaya, India)

Arindan Mandal[1], Thupstan Angchuk[1,2], Mohd Farooq Azam[3], Alagappan Ramanathan[1], Patrick Wagnon[4], Mohd Soheb[1], Chetan Singh[1]

[1]Schola of Environmental Sciences, Jawaharlal Nehru University, New Delhi 110067, India
[2]DST's Centre of Excellence, Department of Geology, Sikkim University, Gangtok 737102, India
[3]Department of Civil Engineering, Indian Institute of Technology Indore, Simrol 453552, India
[4]Université Grenoble Alpes, CNRS, IRD, IGE, F-38000 Grenoble, France

Correspondence to: Arindan Mandal (arindan.141@gmail.com)

Abstract. Analysis of surface energy balance (SEB) at the glacier surface is the most comprehensive way to explain the atmosphere-glacier interactions but that requires extensive data. In this study, we analyse an 11-year (2009-2020) record of the meteorological dataset from an automatic weather station installed at 4863 m a.s.l., on a lateral moraine of the Chhota Shigri Glacier in the western Himalaya. The study was carried out over the winter months (December to April) to understand SEB drivers and snow sublimation. Further, we examine the role of cloud cover on SEB and turbulent heat fluxes. The turbulent heat fluxes were calculated using the bulk-aerodynamic method, including stability corrections. The net short-wave radiation was the primary energy source. However, the turbulent heat fluxes dissipated a significant amount of energy. The cloud cover plays an important role in limiting the incoming short-wave radiation by 70%. It also restricts the turbulent heat fluxes by around 50%, consequently less snow sublimation. During the winter period, turbulent latent heat flux contributed the largest (63%) in the total SEB, followed by net all-wave radiation (29%) and sensible heat flux (8%). Sublimation rates were three times higher in clear-sky conditions than overcast, indicating a strong control of cloud cover in turbulent latent heat flux. Dry air, along with the high snow surface temperature and wind speed, favours sublimation. We also observed that strong and cold winds, possibly through mid-latitude western disturbances, impede sublimation by bringing high moisture content in the region and cooling the snow surface. The estimated snow sublimation fraction was 16-42% of the total winter snowfall at the study site. This indicates snow sublimation is an essential parameter to be considered in the glaciohydrological modelling at the high mountain Himalayan catchments.

1 Introduction

The widespread global glacier imbalance (Slater et al., 2020; Zemp et al., 2019; IPCC, 2019) is a manifestation of ablation dominance compared to accumulation over the last few decades. Ablation processes—including surface melting, sublimation,

evaporation, and wind-driven transport—lead to the loss of snow and ice mass (Bintanja, 1995; Nicholson et al., 2013; Giesen and Andreassen, 2009; Schaefer et al., 2020; Van den Broeke et al., 2005; Oerlemans, 2000; Conway and Cullen, 2016). Among these, sublimation from snow and ice surfaces is one of the significant contributors to the total ablation (Stigter et al.,

35 2018; Huintjes et al., 2015a) yet seldom quantified, especially in the Himalaya-Karakoram (HK) region (Azam et al., 2021). Sublimation can be calculated from the surface energy balance (SEB), which requires several meteorological inputs to describe the physical relationship between the glacier/snow surface and meteorological variables (Oerlemans, 2001).

SEB studies are rare in the HK region due to the extreme terrain and the lack of high-altitude meteorological data from glacier and snow-covered sites. SEB studies have been conducted on nearly eleven glacier/snow-covered sites across the HK region

40 (see supplementary material; Table S1 and Fig. S1). However, SEB studies on Tibetan glaciers are relatively more (~17 investigated glaciers/ice-covered sites; Table S1), including direct turbulent heat flux measurements (Yang et al., 2011; Zhu et al., 2018). In the HK region, a few SEB experiments have been carried out recently, most of them being in the central Himalaya in Nepal, yet at a smaller temporal range, from a month to a few seasons/years (Rounce et al., 2015; Steiner et al., 2018; Acharya and Kayastha, 2019; Litt et al., 2019; Matthews et al., 2020; Steiner et al., 2021). SEB studies in the Indian

45 Himalaya are few. Only a single on-glacier SEB experiment was conducted at the Chhota Shigri Glacier in the western Himalaya (Azam et al., 2014a). Recently, Singh et al. (2020) conducted a SEB experiment on a moraine surface with ephemeral snow cover near the Pindari Glacier in Uttarakhand using two-year data from a weather station.

Apart from the limited number of SEB sampled sites in the HK, the available literature mostly focused on the radiative or net radiation fluxes. Net radiation plays a greater role in supplying melt energy to snow/ice than turbulent heat fluxes (Smith et

50 al., 2020). Turbulent fluxes can contribute about 20% of SEB globally and sometimes above 70% for a shorter timescale (Thibert et al., 2018). The higher contribution of turbulent heat flux is common in the high-latitudinal glaciers having low altitude, where snow-ice surfaces are exposed to high air temperatures and dry conditions. The contribution of turbulent heat fluxes in some Tibetan and Nepalese glaciers/snow-covered sites are also higher, well larger than 20%, e.g., Chongche Ice Cap in the Kunlun Mountains, South Col of the Everest (Table S1). The SEB experiment on the Everest summit shows a

55 decrease in turbulent heat flux boosts short-wave radiation efficiency, resulting in surface melting despite air temperature below freezing (Matthews et al., 2020). Overall, the turbulent heat flux and their involvement in SEB of the HK glaciers are rarely studied and fairly understood.

Snow sublimation is expected to be a significant component of the glacier surface mass balance in the HK (Azam et al., 2021). Stigter et al. (2018) showed that sublimation loss on the Yala Glacier, central Himalaya/Nepal is larger than 20% of winter

60 snowfall. Sublimation contribution is even higher, up to 66% of the total mass loss on the Purogangri ice cap, Tibetan Plateau (Huintjes et al., 2015b). Recently, Gascoin (2021) reported that the basin-wide mean snow sublimation is ~11% of the total snow ablation in the Indus basin, with > 60% in Ladakh and western Tibet areas based on satellite-derived datasets (HMASR v1). The HK region's high-altitude conditions, i.e., high wind, low atmospheric pressure, and dry air, are expected to support sublimation (Wagnon et al., 2013; Shea et al., 2015; Mandal et al., 2020; Matthews et al., 2020; Azam et al., 2018). Therefore,

65 the quantification of high-altitude sublimation is important to improve our understanding of the mass balance components in the HK region.

Direct sublimation measurement requires the use of an eddy covariance system or pan sublimation technique. The eddy covariance system is advanced and precise (Sexstone et al., 2016) but expensive, hence it has been used only in two studies in the HK region, e.g., Yala and Lirung glaciers in Nepal (Stigter et al., 2018; Steiner et al., 2018). The pan sublimation
70 measurements have not been conducted in the HK region, likely due to accessibility and harsh weather conditions. Alternatively, the bulk-aerodynamic method is widely used for calculating turbulent heat fluxes and sublimation. On the Yala Glacier, Stigter et al. (2018) evaluated multiple methods (e.g., bulk-aerodynamic, the Penman-Monteith equation and an empirical relation) with eddy covariance-based sublimation. Results show that the bulk method estimate is similar to observed eddy covariance-based sublimation. However, parameterisation of the bulk-exchange coefficient and surface roughness length
75 is critical for precisely modelling the turbulent heat fluxes (Smith et al., 2020; Stigter et al., 2018).

We present an 11-year long SEB study on the snow-covered side moraine of the Chhota Shigri Glacier in the western Himalaya using an off-glacier automatic weather station (AWS) at 4863 m a.s.l. The AWS records the year-round data, but for this study, we considered the snow-covered period between December and April of each hydrological year between 2009 and 2020. Our primary focus is to better understand the turbulent heat fluxes and their role in SEB during the winter season when the
80 atmospheric conditions are windier and drier. We also quantified the snow sublimation and its meteorological drivers. We have given special attention in identifying the role of cloud cover on the SEB components and sublimation. Finally, we estimated the fraction of snow sublimation to the winter snowfall at the AWS site.

2 Study area and AWS

2.1 Chhota Shigri moraine site and AWS description

85 Chhota Shigri Glacier is located in the Chandra basin (sub-basin of the Indus), Lahaul-Spiti valley, western Himalaya (Fig. 1). The Chandra basin (~30% glacierised) is located in the monsoon-arid transition zone and is influenced by the Indian Summer Monsoon (ISM) during summer and the Western Disturbances (WDs) during winter (Bookhagen and Burbank, 2010). The mean annual precipitation at the Chhota Shigri base camp was 922 mm, of which 67% was during the winter season (November-April) and the remaining 33% during the summer-monsoon (May-October) (Mandal et al., 2020). Chhota Shigri
90 is among the most-studied glaciers in the HK region in terms of surface mass balance and glacial processes. The mean annual glacier-wide mass balance was -0.46 ± 0.40 m w.e. a^{-1} (water equivalent) over 2002-2019 (Mandal et al., 2020). Azam et al. (2014a) carried out a SEB experiment on this glacier using an on-glacier AWS during 2012-2013 but could not conduct a full-year SEB analysis due to AWS failure in winter (AWS-G in Fig. 1). They estimated that the net all-wave radiation (R_{net}) was the primary energy source with about 80% energy flux to SEB, while the turbulent and ground heat flux shared the rest of the
95 total heat flux.

For this study, meteorological data were collected on the side moraine of the Chhota Shigri Glacier using an AWS (AWS-M; 32.23° N, 77.51° E) installed at 4863 m a.s.l. (Fig. 1). AWS-M is located ~50 m away from the Chhota Shigri Glacier margin and on a relatively flat hill-top site. The surface at the AWS-M site remains snow-covered during winter and bare-sand/sediment exposed during summer (Fig. 1). AWS-M has been operating since October 2009. Air temperature (T_{air}), surface temperature (T_s), relative humidity (RH), wind speed (u) and direction (WD), incoming and outgoing short-wave (S_{in} and S_{out}) and long-wave (L_{in} and L_{out}) radiations were being recorded at a frequency of 30 seconds and stored as half-hourly averages by a Campbell CR1000 data logger. Data before 23 May 2010 was recorded at hourly time-step. Precipitation was recorded at the base camp at 3850 m a.s.l. using a Geonor-T200B sensor since July 2012. Description and specifications of the sensors for AWS-M and Geonor gauge are provided in Table 1.
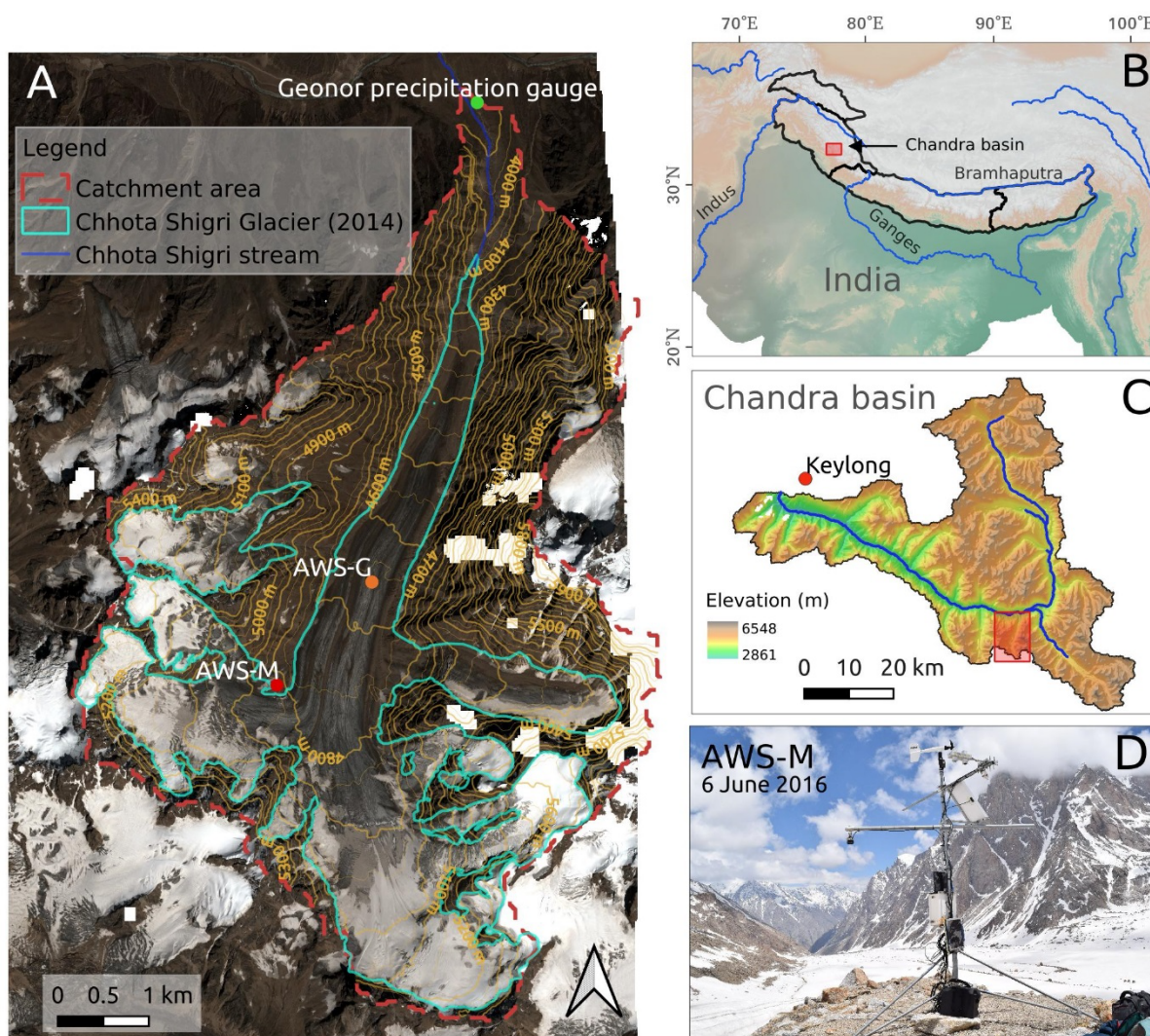

4

Figure 1. (A) Chhota Shigri Glacier catchment showing the location of the AWS-M (red dot), AWS-G (orange dot; middle ablation zone) and Geonor T-200B automatic precipitation gauge (green dot). Glacier outline was derived using the 2014 Pléiades image (Azam et al., 2016). The background is the Pléiades ortho-image of 12 September 2020 (copyright CNES 2020, distribution Airbus D&S). (B) Location of the Chhota Shigri Glacier region in the western
110 **Himalaya. (C) Map of the Chandra basin, with Chhota Shigri catchment marked (red rectangle). Elevation based on the Shuttle Radar Topographic Mission (SRTM) Digital Elevation Model (DEM) obtained from the United States Geological Survey (USGS). (D) Photo of the AWS-M on the lateral moraine (Photo credit: A Mandal).**

Table 1. Details of the AWS-M (4863 m a.s.l.) and Geonor precipitation gauge at the base camp (3850 m a.s.l.) of the Chhota Shigri Glacier. Variable symbols are also given. Sensor heights indicate the distances to the surface without
115 **snow. Long-wave radiation sensors have been operational since May 2010. The snow depth sensor was operational until October 2015.**

Meteorological variable	Symbol (unit)	Sensor	Height (m)	Accuracy
AWS-M				
Air temperature	T_{air} (°C)	Campbell H3-S3-XT	1.5	±0.1 at 0 °C
Surface temperature	T_s (°C)	Apogee SI-111[a]	2.5	±0.2 (-10 to +65 °C) ±0.5 (-40 to +70 °C)
Relative humidity	RH (%)	Campbell H3-S3-XT	1.5	±1.5% RH at 23 °C
Wind speed	u (m s^{-1})	Campbell 05103-10-L	3	±0.3 m s^{-1}
Wind direction	WD (degree)	Campbell 05103-10-L	3	±3 degree
Incoming and outgoing short-wave radiations	S_{in}, S_{out} (W m^{-2})	Kipp & Zonen CNR-1	2.5	±10% day total
Incoming and outgoing long-wave radiations	L_{in}, L_{out} (W m^{-2})	Kipp & Zonen CNR-1	2.5	±10% day total
Snow depth	SR50A (m)	Campbell SR50A	2	±0.01 m or 0.4% to target
Precipitation	P (mm)	Geonor T-200B	1.7[b]	±0.6 mm

Infrared radiometer; [b]Inlet height

3 Datasets and methodology

3.1 Meteorological data and gaps

120 Meteorological data from the AWS-M is used between 1 December and 30 April (DJFMA) of each hydrological year for 2009-2020. We filter the snow-covered period for SEB based on the surface albedo threshold value above 0.4 at the AWS-M (the mean bare-ground/snow-free surface albedo was < 0.25 for July-August; 2009-2020). Additionally, we discarded data of 74 days (2975 data points) out of total 1664 days (76248 data points; 2009-2020) when albedo was below 0.4 (refer to Table S2 for snow-free dates). This albedo threshold value is similar to the minimum albedo (0.41 to 0.46) of continuous snow cover at
125 the Ganja La and Yala sites in Nepal (Stigter et al., 2021; Kirkham et al., 2019).

There was a gap in observation of all variables in the AWS-M data during the night (18:00 to 06:00 Indian Standard Time; IST) between 22 February 2015 and 2 October 2016 (220 days of DJFMA) due to a disconnected wire between the solar panel and the battery. These gaps were filled using the mean value of the respective variables from available records (1 December 2009 – 21 February 2015 and 1 December 2016 – 30 April 2020) of the AWS-M for the particular time-steps on the same day.

130 To identify the reliability of the gap-filling method, we applied the same method for non-missing year data by removing the night values (18:00-06:00 IST) and filled them with mean values from other years. The root mean square error (RMSE) and mean absolute error (MAE) between the original (with night values) and the filled dataset was found to be 3.3°C and 2.6°C for T_{air}, 4.1°C and 3.3°C for T_s, 27% and 22% for RH, and 2.7 m s^{-1} and 2.1 m s^{-1} for u, respectively for the test year, 2017/18.

Precipitation data was used from the single-alter-shielded Geonor gauge operated at the glacier base camp at ~3850 m a.s.l.
135 since July 2012 (Fig. 1). All-weather rain gauges are known to undercatch precipitation in case of snow (Kochendorfer et al., 2017), and since our measurements have not been corrected yet, we suspect that precipitation magnitude is underestimated during the snow season (i.e., winter, spring). But those values have only been used to compare with cumulative sublimation in corresponding years, and this does not impact our results. Geonor gauge has a data gap between October 2013 and July 2014 due to battery failure. Therefore, for the gap period, we used monthly precipitation records from the nearest Indian
140 Meteorological Department's (IMD) Keylong station at 3119 m a.s.l. (https://weathershimla.nic.in/en-IN/climatedata.html, last access: 15 November 2021). Keylong data is used because it is the only existing observatory close to the study area (~60 km from the AWS-M site; Fig. 1). Geonor and Keylong precipitation gauges cannot differentiate between snow and rain. Since the daily and monthly T_{air} did not rise above 0°C during DJFMA (Fig. 2; Table 2), we considered DJFMA precipitation as snowfall at both sites. Moreover, the AWS-M site is located 1013 m higher than the Geonor gauge altitude. The measured
145 precipitation of Geonor and Keylong were well correlated (R^2 = 0.82); however, the RMSE was higher: 274 mm (Fig. S2). Therefore, we applied a precipitation gradient of 0.1 m km^{-1} following Azam et al. (2014b) to extrapolate Keylong's precipitation to the AWS-M altitude.

3.2 Surface energy balance (SEB)

SEB is calculated at a point location for the skin layer using the AWS-M data at a half-hourly time-step between 1 December
150 and 30 April (~151 days) of each hydrological year between 2009 and 2020 (hourly time-step for 2009/10). The SEB at the snow surface can be written as (Van den Broeke et al., 2005; Hock, 2005; Oke, 1987):

$$F_{surface} = S_{net} + L_{net} + H + LE + G + P,\qquad(1)$$

where $F_{surface}$ [W m^{-2}] is the net energy balance of all energy fluxes at the snow surface, S_{in} and S_{out} are the incoming and outgoing short-wave radiation, L_{in} and L_{out} are the incoming and outgoing long-wave radiation, H and LE are the sensible and
155 latent turbulent heat fluxes, G and P are the subsurface heat flux and heat advected by precipitation, respectively.

Compared to other fluxes, P on glacier/snow is negligible (Hock, 2005; Kayastha et al., 1999) therefore neglected here. G was found to be negligible or close to 0.0 ± 1.0 W m^{-2} at the on-glacier AWS-G site on the Chhota Shigri Glacier during winter 2012/13 (Azam et al., 2014a), thus neglected in the present study. Also, G was neglected in SEB of transient snow cover at the Ganja La and Yala site in Nepal, considering inadequate measurement and information of potentiality of G in the HK

region (Stigter et al., 2021). All fluxes are expressed in W m^{-2} and defined as positive when directed towards the surface and negative when away from the surface.

3.2.1 Radiative fluxes

S_{net} [W m^{-2}] and L_{net} [W m^{-2}] are represented as S_{in} - S_{out} and L_{in} - L_{out}, respectively and all together can be expressed as net radiation, $R_{net} = (S_{net} + L_{net})$. However, several corrections were applied to S_{in} and S_{out} datasets before using them for SEB. All the night values (determined based on solar elevation angle) of S_{in} and S_{out} were set to be zero. The measured S_{out} was higher than S_{in} (1.6 % of total data) during the morning and evening time. Mainly due to the low solar angle because of poor cosine response of the upward-looking pyranometer (S_{in}) or due to covering up of the pyranometer by snowfall (Nicholson et al., 2013; Favier et al., 2004). In such cases, S_{in} was corrected using S_{out} (raw) and accumulated albedo (α_{acc}) (Van den Broeke et al., 2004). α_{acc} is the 24-hour sum of S_{out} divided by the sum of S_{in} centred around the moment of observation and calculated following Van den Broeke et al. (2004):

$$\alpha_{acc} = \frac{\sum_{24} S_{out}}{\sum_{24} S_{in}}, \tag{2}$$

L_{net} was calculated from the difference between observed L_{in} and L_{out} . We used raw data from up and down pyrgeometers (CG3) of the radiation sensor (CNR-1) to compute the final L_{in} and L_{out} at the AWS-M site.

3.2.2 Turbulent energy flux

The vertical turbulent heat fluxes, H and LE, are calculated using the bulk-aerodynamic method, including stability correction (Brutsaert, 1982). This method is widely used for its applicability because it allows estimating H and LE from one level of measurement (Chambers et al., 2020; Radić et al., 2017). The bulk-aerodynamic method has already been applied on this glacier at the AWS-G site (on-glacier; Fig. 1) to conduct a SEB experiment during 2012/13, where the SEB model result showed a good agreement with observed surface melt (Azam et al., 2014a). Further, the bulk method showed a good agreement compared to the eddy covariance observations over a snow-covered central Himalayan glacier (Stigter et al., 2018). In addition, Denby and Greuell (2000) showed that the bulk-aerodynamic method gives reasonable results in high wind speeds, even in katabatic wind conditions. Therefore, the bulk-aerodynamic method is applied in the present study as it has already been applied in this glacier and several studies in the HK region, where atmospheric conditions are similar with high winds (Litt et al., 2019; Stigter et al., 2021; Azam et al., 2014a).

The bulk Richardson number, R_{ib}, describes the stability of the surface layer (Eq. 3), which relates the relative effects of buoyancy to mechanical forces (e.g., Brutsaert, 1982). Therefore, the stability effects were accounted based on R_{ib}:

$$R_{ib} = g \frac{\frac{(T_{air}-T_s)}{(z_t-z_{0t})}}{T_{air}(\frac{u}{z_u-z_{0m}})^2}, \tag{3}$$

where g is the acceleration due to gravity [g = 9.81 m s^{-2}]; T_{air} and u are the air temperature [in K] and horizontal wind speed [in m s^{-1}] at the measurement height, respectively; T_s is the surface temperature [in K]. z_u and z_t are the measurement heights

190   [m] for wind speed and air temperature, respectively. z_{0m}, z_{0t} and z_{0q} are the surface roughness lengths [m] for momentum, temperature and humidity, respectively. R_{ib} is positive in a stable atmosphere. Assuming that local gradients of mean horizontal wind speed, temperature and specific humidity are equal to the finite differences between the measurement height and the surface, the turbulent fluxes, H and LE are (Brutsaert, 1982):

$$H = \rho \frac{C_P k^2 u (T_{air} - T_s)}{\ln(\frac{z_u}{z_{0m}}) \ln(\frac{z_t}{z_{0t}})} (\Phi_m \Phi_h)^{-1},$$ (4)

195

$$LE = \rho \frac{L_s k^2 u (q - q_s)}{\ln(\frac{z_u}{z_{0m}}) \ln(\frac{z_t}{z_{0q}})} (\Phi_m \Phi_v)^{-1},$$ (5)

where ρ is the air density at 4863 m a.s.l. [in kg m^{-3}] calculated as $\rho = \rho_0 \frac{p_{air}}{p_0}$ where ρ_0 is the density [in kg m^{-3}] at standard sea level pressure p_0 [1013.25 kPa] and p_{air} is atmospheric pressure [in Pa] measured at the site (Cuffey and Paterson, 2010). C_P is the specific heat capacity of air [in J kg^{-1} K^{-1}] (C_p = C_{pd} (1+0.84q) with C_{pd} = 1005 J kg^{-1} K^{-1}, the specific heat capacity for dry air at constant pressure), L_s is the latent heat of sublimation for T_s < 0 °C (2.849 × 10^6 J kg^{-1}), q and q_s [kg kg^{-1}] are the

200   specific humidity at height z and surface, respectively. q and q_s were calculated using measured T_{air}, T_s and RH. $\Phi_{m/h/v}$ are the non-dimensional stability functions for momentum, heat, and vapor/moisture, respectively. The stability functions are given by Brutsaert (1982) and previously applied in several glacier SEB studies (e.g., Reid and Brock, 2010) and on the Chhota Shigri Glacier (Azam et al., 2014a). $\Phi_{m/h/v}$ expressed in terms of R_{ib}:

For R_{ib} > 0 (stable case):

205

$$(\Phi_m \Phi_{h/v})^{-1} = (1 - 5R_{ib})^2,$$ (6)

For R_{ib} < 0 (unstable case):

$$(\Phi_m \Phi_{h/v})^{-1} = (1 - 16R_{ib})^{0.75},$$ (7)

Half-hourly data of u, T_{air}, T_s and RH were used to apply the bulk-aerodynamic method when the AWS-M surface was snow-covered (α_{acc} > 0.4). T_s was directly used from the measurement by an infrared radiometer (Table 1). The correlation between

210   infrared measured T_s and T_s derived from L_{out} (using Stefan-Boltzmann equation for a black body/snow surface with emissivity of 0.99) was R^2 = 0.99 (p < 0.001) with RMSE = 0.36°C. The lower and upper limits of R_{ib} were fixed at -0.40 and 0.23, respectively, beyond which all turbulence is suppressed (Denby and Greuell, 2000; Favier et al., 2011). In this way, we discarded about 11% of the data points beyond the R_{ib} range.

The aerodynamic (z_{0m}) and scalar surface roughness lengths (z_{0t}) play a pivotal role in the bulk method as the turbulent fluxes

215   are very sensitive to the choice of these surface roughness lengths (Chambers et al., 2020; Smith et al., 2020; Nicholson and Stiperski, 2020; Wagnon et al., 1999). Therefore, in this study z_{0m} for snow surface is taken as 0.001 m which was calculated

for the AWS-G site between 16 September 2012 and 17 January 2013 when the AWS-G surface was snow-covered (Azam et al., 2014a). This value was calculated using wind measurements at two different levels following a conventional logarithmic profile (e.g., Moore, 1983). Similarly, z_{0t} and z_{0q} for snow surface is considered 0.001 m following Azam et al. (2014a).

220 Sublimation (S) was estimated for every DJFMA period between 2009 and 2020 (excluded days are listed in Table S2). S [10^{-3} kg m^{-2} or mm w.e.] was calculated at a half-hourly time-step (hourly time-step for 2009/10) from LE, when it was negative, according to:

$$S = \frac{LE \, dt}{L_s},$$ (8)

where L_s denotes latent heat of sublimation and dt is the time-step [in seconds].

3.3 Cloud factor

Cloud cover is a good indicator of the radiation contribution to the surface (Favier et al., 2004). In this study, the cloud factor (CF) is calculated at the AWS-M site between 09:00 and 16:00 IST to avoid the steep valley wall's shading effect during morning and evening time. CF is calculated by comparing short-wave incoming (S_{in}) with the short-wave radiation at the top of the atmosphere (S_{TOA}) following equation by Favier et al. (2004):

230
$$CF = 1.3 - 1.4 \left(\frac{S_{in}}{S_{TOA}} \right),$$ (9)

which represents a quantitative cloud cover estimate and ranges from 0 to 1. The values 1.3 (offset) and 1.4 (scale factor) were derived from a simple linear optimisation process (Favier et al., 2004). S_{in} was used from the direct measurement from the AWS-M, whereas the theoretical value of S_{TOA} for a horizontal surface is calculated following Iqbal (1983).

3.4 Statistical analysis

235 The standard correlation coefficient (r) and coefficient of determination (R^2) were estimated to assess the relationship between various meteorological variables, SEB and sublimation. The two-tailed Student t-test was used to measure the significance of the r and R^2. RMSE is calculated to identify the bias/deviation. The K-fold cross-validation method was applied for linear and multiple regression analysis, performed using the 'caret' package (Kuhn, 2021) of the R environment (R Core Team, 2021). Cross-validation is a machine learning technique that is used to protect the predictive model against overfitting for better 240 accuracy. We used this method to estimate the meteorological parameter's variance in sublimation.

4 Results

4.1 DJFMA meteorological characteristics

The range of the meteorological variables measured at the AWS-M for DJFMA (2009-2020) is given in Table 2 to provide an
245 overview of the prevailing weather conditions in the study region. During DJFMA, the mean monthly T_{air} ranged from -15.5°C
in January to -6.9°C in April, with a mean of -12.1°C. T_{air} was below 0°C except during late April in 2010/11 and 2016/17
when daily T_{air} slightly exceeded 0°C (Fig. 2). The highest daily T_{air} was 0.1°C on 27 April 2011 and the lowest was -21.9°C,
on 26 January 2019. The mean monthly T_s ranged from -17.7°C in January to -7.5°C in April, with a mean of -13.7°C. Daily
T_s was below 0°C across DJFMA; however, half-hourly T_s was higher than T_{air} for about 45% of the data points.

250 The mean monthly RH ranged from 31% in January to 49% in April, with a mean of 43%. However, the daily RH was higher
than 60% across DJFMA, but for a few days. The daily mean RH was below 30% (assumed as dry air) for 29% of days and
above 60% (humid air) for 24% of days during the study period.

The mean monthly u ranged from 3.7 m s^{-1} in April to 6.0 m s^{-1} in February, with a mean of 5.0 m s^{-1} during DJFMA. Based
on half-hourly records, $u < 5.0$ m s^{-1} occurred for 56% of the time during the study period, while $u > 10.0$ m s^{-1} were observed
255 for only 7% of the time. The half-hourly mean u reaches up to 24.2 m s^{-1} on 21 February 2019. The highest recorded daily
mean u was 15.9 m s^{-1} (20 March 2012). The windrose shows that there is a persistent down-valley wind (along the glacier
flowline) coming from the south-east (90°-135°) across DJFMA with the strong and cold wind (Fig. 3). The second dominant
direction was from the west but with relatively lower speeds.

Precipitation records from the Geonor gauge were available only for five complete DJFMA periods (Fig. 4). During DJFMA,
260 most of the precipitation in the Chhota Shigri catchment falls due to the WDs cyclonic storms, accounting for about 67% of
its annual total of ~900 mm (Mandal et al., 2020). The total mean precipitation during DJFMA was 659 mm (2012-2018; Table
2). March received the highest, with 150 mm corresponds to 26% and least in December, with 56 mm. The observed highest
single-day precipitation was 61 mm w.e. recorded on 30 March 2015.

Table 2. Monthly mean and range of observed meteorological and SEB variables at the AWS-M for DJFMA, 2009-
265 **2020. Precipitation records from the glacier base camp are between 12 July 2012 and 30 April 2018.**

Variable	Dec	Jan	Feb	Mar	Apr	Min.	Max.	Mean
Meteorology								
T_{air} (°C)	-13.0	-15.5	-14.2	-11.0	-6.9	**-21.9**	**0.0**	**-12.1**
T_s (°C)	-16.2	-17.7	-15.1	-11.9	-7.5	**-27.4**	**0.6**	**-13.7**
RH (%)	32	41	49	45	49	**10**	**99**	**43**
q (g kg^{-1})	0.8	0.8	1.1	1.3	2.0	**0.2**	**4.3**	**1.2**
u (m s^{-1})	5.3	5.4	6.0	4.6	3.7	**0.7**	**15.9**	**5.0**
S_{TOA} (W m^{-2})	212	226	261	301	343	**211**	**447**	**303**

S_{in} (W m^{-2})	124	135	165	236	293	**28**	**414**	**191**
S_{out} (W m^{-2})	70	82	107	158	197	**21**	**286**	**123**
L_{in} (W m^{-2})	181	191	208	213	226	**123**	**290**	**204**
L_{out} (W m^{-2})	249	243	253	266	285	**207**	**319**	**260**
α_{acc}[§]	0.59	0.63	0.68	0.69	0.69	**0.22**	**0.94**	**0.66**
CF[§]	0.46	0.46	0.47	0.36	0.33	**0.06**	**0.99**	**0.41**
P (mm)	56	109	135	150	119	-	-	**569**[V]
P (%)[+]	10	19	24	26	21	-	-	**100**
SEB								
S_{net} (W m^{-2})	54	52	58	78	97	**4**	**207**	**68**
L_{net} (W m^{-2})	-68	-52	-45	-54	-58	**-129**	**18**	**-55**
R_{net} (W m^{-2})	-11	2	15	26	41	**-50**	**124**	**15**
H (W m^{-2})	8	1	-6	-12	-12	**-118**	**102**	**-4**
LE (W m^{-2})	-35	-30	-37	-42	-47	**-145**	**0**	**-38**
$H+LE$ (W m^{-2})	-27	-29	-42	-49	-54	**-204**	**73**	**-40**
F (W m^{-2})	-38	-27	-28	-28	-18	**-151**	**127**	**-28**

[§]Mean values between 09:00 and 16:00 IST and values are rounded to 2 decimal places;
[V]Sum of DJFMA precipitation (see Fig. 4);
[+]Sum of DJFMA monthly values.
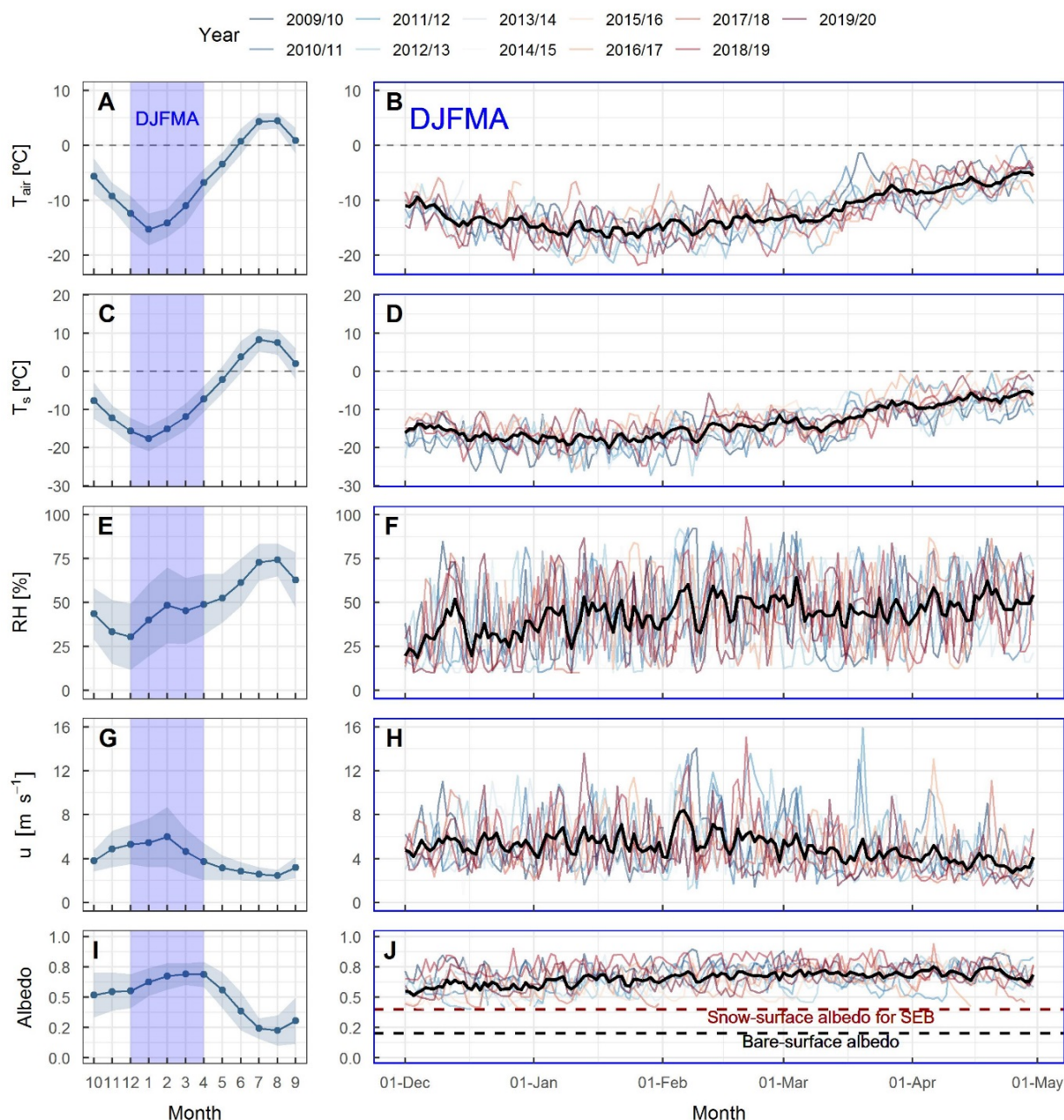
Figure 2. Monthly climatology (left panels) and daily averages (right panels; 1 December to 30 April) of half-hourly measurements of air (T_{air}) and surface temperature (T_s), relative humidity (RH), wind speed (u) and surface albedo (α_{acc}) at the AWS-M for 2009-2020. Snow-surface albedo (α_{acc} = 0.4) for SEB analysis and bare-surface albedo (α_{acc} = 0.2) are also shown in the albedo panel (J). Light blue shade in the monthly climatology represents the period between December and April. The shades in the monthly climatology plots represent the standard deviation (SD) of respective variables. The bold black line in the daily panel highlights the mean of all years.
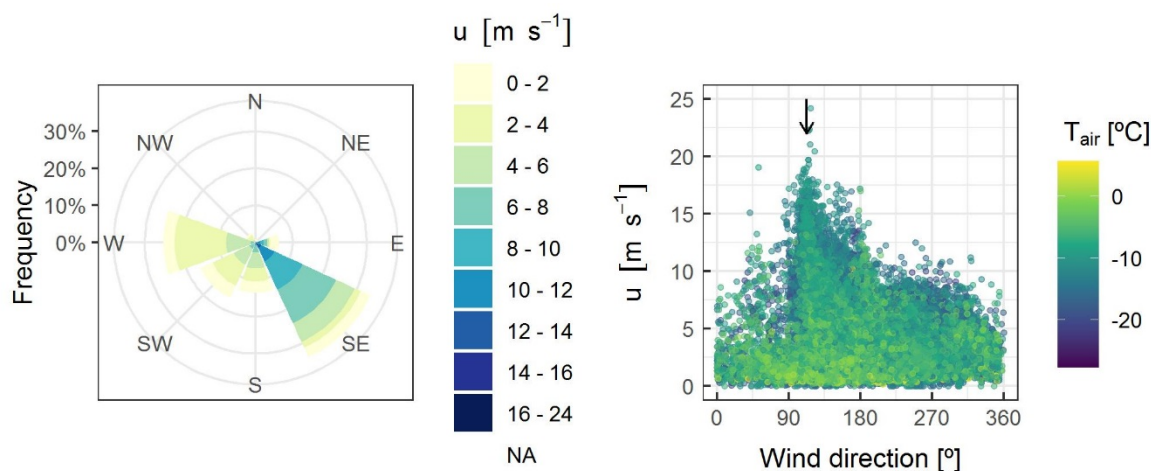
Figure 3. Windrose of the AWS-M and scatter plot of wind speed vs direction with air temperature shown in the colour bar for DJFMA (2009-2020). The frequency of wind direction is expressed as a percentage for n = 69666 half-hourly data points. The arrow in the scatter plot indicates the direction of the local flowline.
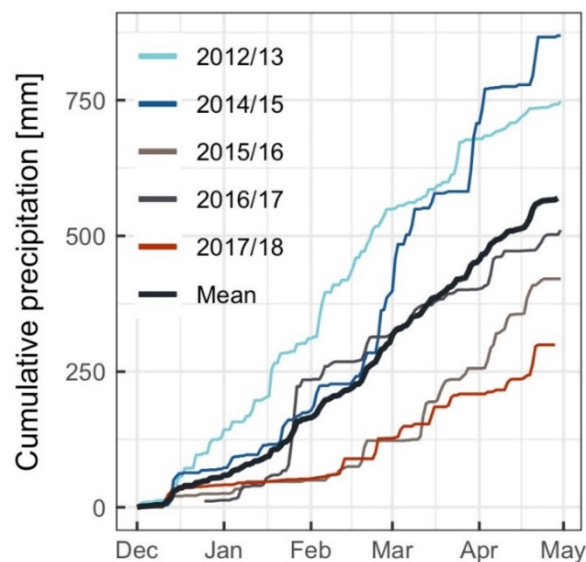

Figure 4. Cumulative precipitation at the glacier base camp at 3850 m a.s.l. for DJFMA, 2012-2018. No data for 2013/14. The bold line is the mean of all years.

285

13

The Cryosphere

Discussions

Open Access

EGU

4.2 Surface radiation fluxes

The daily mean variability of radiation components and CF at the AWS-M for DJFMA (2009-2020) is shown in Fig. 5. About 62% of S_{TOA} reached the surface at the AWS-M during the study period, indicating the remainder was absorbed and scattered by the cloud cover and atmospheric constituents (e.g., gases, water vapour). Daily mean S_{in} varies between 28 and 414 W m^{-2},

290 corresponding to a mean of 191 W m^{-2} (Table 2). The highest half-hourly instantaneous S_{in} was higher than 1300 W m^{-2} for five data points in April. Such high S_{in} values were previously observed at high-altitude catchments of the mid-latitude (~30°N) region (e.g., Wani et al., 2021; Matthews et al., 2020). This could be due to multiple reflections from nearby snow covers and thin clouds (de Kok et al., 2019). S_{in} was highest in April with a daily mean of 295 W m^{-2}. The persistent snow cover, especially during the peak winter period across the study period, resulted in a strong reflection of S_{in} radiation (Fig. 5). S_{out} was the largest

295 (α_{acc} = 0.69) in March-April because of the accumulated snow cover. L_{in} follow the CF pattern (Fig. 5). Low L_{in} attributed to the low CF (clear-sky) conditions. Daily mean L_{in} varies between 123 and 290 W m^{-2}, corresponding to a mean of 203 W m^{-2} (Table 2). The highest L_{in} received in April with a daily mean of 226 W m^{-2}. L_{out} was relatively stable across DJFMA, ranging from 243 W m^{-2} to 285 W m^{-2} with a mean of 260 W m^{-2} (Table 2). S_{net} follows the pattern of S_{in} in all years with a mean of 68 W m^{-2} (Fig. 5). L_{net} do not show much variability across DJFMA, with a mean of -55 W m^{-2} for the study period (Fig. 5).
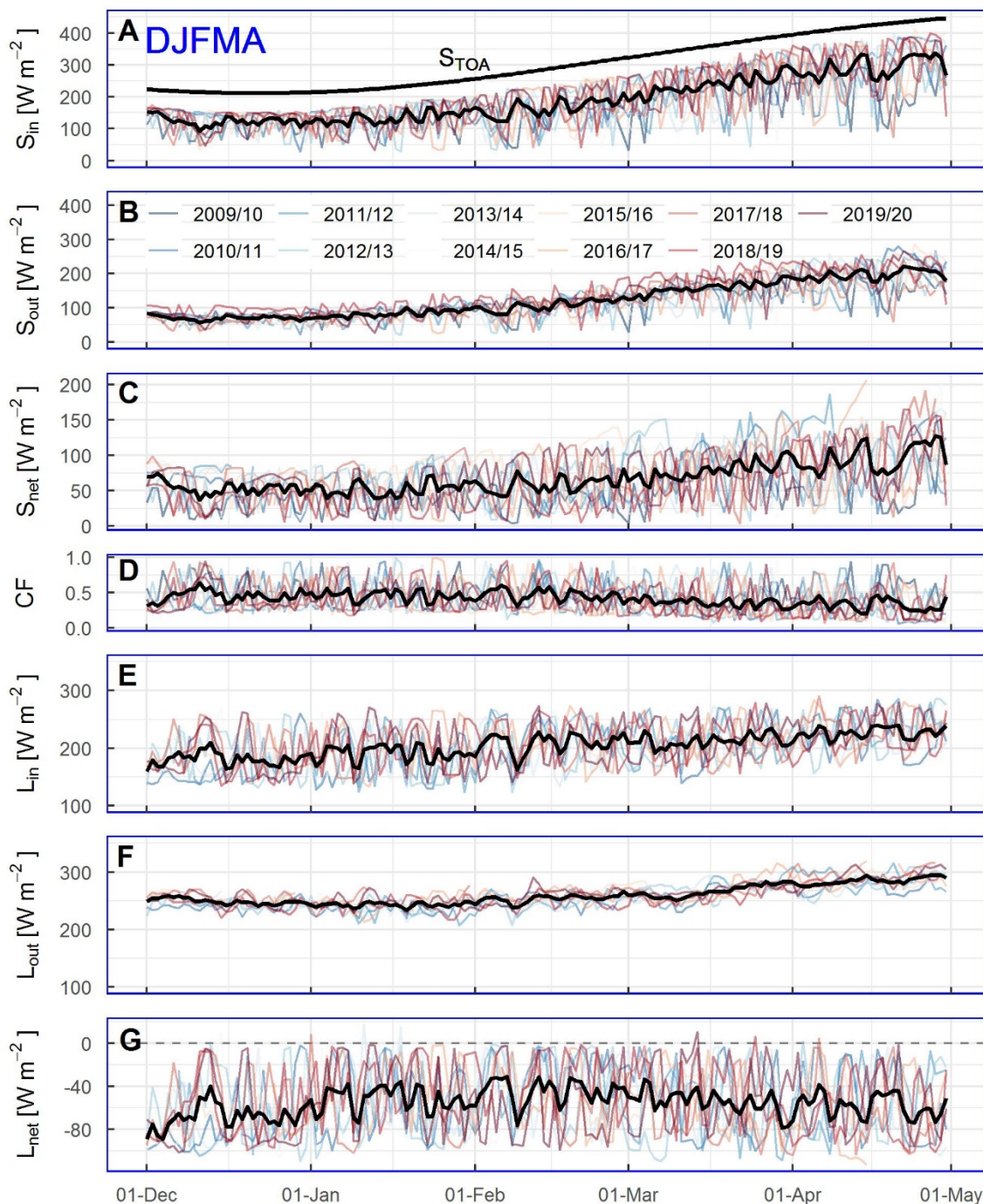
Figure 5. The daily mean of short-wave radiation at the top of the atmosphere (S_{TOA}; in W m^{-2}), short-wave incoming (S_{in}), outgoing (S_{out}) and net (S_{net}), cloud factor (CF), long-wave incoming (L_{in}), outgoing (L_{out}) and net (L_{net}), and net all-wave radiation (R_{net}) at the AWS-M for DJFMA, 2009- 2020. L_{in} starts from 1 December 2010. The bold black line highlights the mean of all years.

300

4.3 SEB fluxes

305

The daily R_{net} ranged from -50 to 124 W m^{-2} with a mean of 15 W m^{-2} (Table 2). R_{net} was negative in December with a mean of -11 W m^{-2}, which gave rise to near-surface air cooling. R_{net} acted as a heat supplier from February to April with a mean value of 15, 26 and 41 W m^{-2}, respectively (Fig. 6). The daily H ranged from -118 to 102 W m^{-2} with a mean of -4 W m^{-2} (Table 2). H was positive for 56% of the half-hourly values suggesting the atmosphere transported heat towards the surface.

310 The daily H was negative (44% of the half-hourly values) between February and March up to -118 W m^{-2}. The mean daily LE ranged from -145 to 0 W m^{-2}, with a mean of -38 W m^{-2} (Fig. 6; Table 2). LE was always negative across DJFMA (except 2% of the half-hourly values), suggesting mass loss through sublimation (refer to Sect. 4.7). R_{net} played an essential role in governing the turbulent fluxes. For example, the daily H was positive in December with 8 W m^{-2} but gently shifted to a negative value up to -12 W m^{-2} with the progression of winter when R_{net} was significantly larger with warmer temperatures (Table 2).

315 Together, $H+LE$ contributed a negative budget across DJFMA with a mean daily value of -40 W m^{-2}. As a result, the residual energy of SEB ($F_{surface}$) was negative across DJFMA. $F_{surface}$ followed a similar temporal oscillation as R_{net} (Fig. 7). The mean daily $F_{surface}$ ranged from -151 to 127 W m^{-2} with a mean of -28 W m^{-2} during the study period (Table 2).

Fig. 7 presents the contributions of energy fluxes to SEB. During the study period, the proportional contribution of all SEB components showed that LE dominated the contribution (63%), followed by R_{net} (29%) and H (8%). LE (negative) acted as a

320 heat sink while both R_{net} and H were the heat sources to the snow surface. The mean monthly contribution showed an increasing contribution of R_{net} with decreasing LE and H (Table 2). The largest contribution of R_{net} in SEB is well noted across the HMA glaciers (Table S1). However, in this study during the winter season, such a higher contribution of LE (> 60%) is unique and contrary to the previous findings (e.g., Zhang et al. 2013). A higher magnitude of LE is responsible for high snow sublimation (Sect. 4.7).
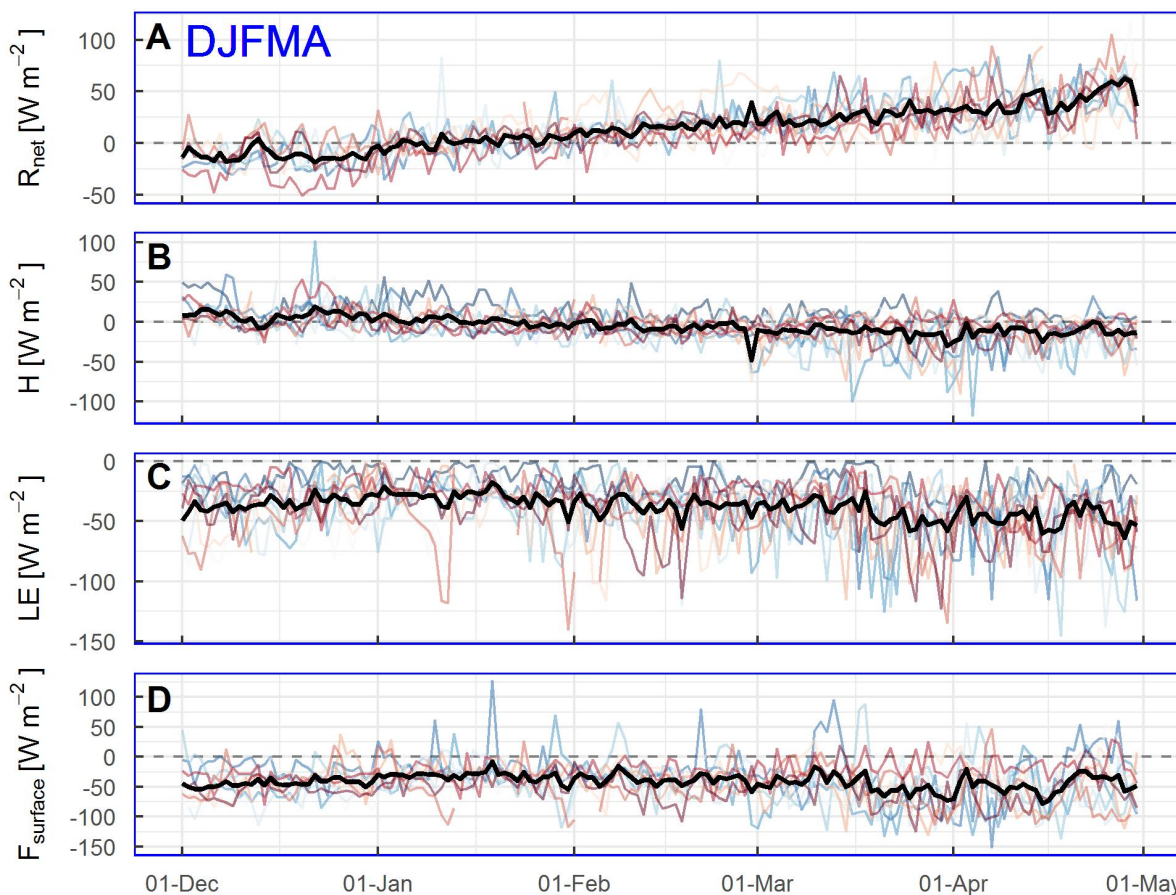
Figure 6. Same as Figure 5 but for net radiation (R_{net}), sensible heat (H), latent heat (LE) and residual energy at the surface ($F_{surface}$) at the AWS-M for DJFMA, 2009-2020. R_{net} and $F_{surface}$ start from 1 December 2010. The bold black line highlights the mean of all years.
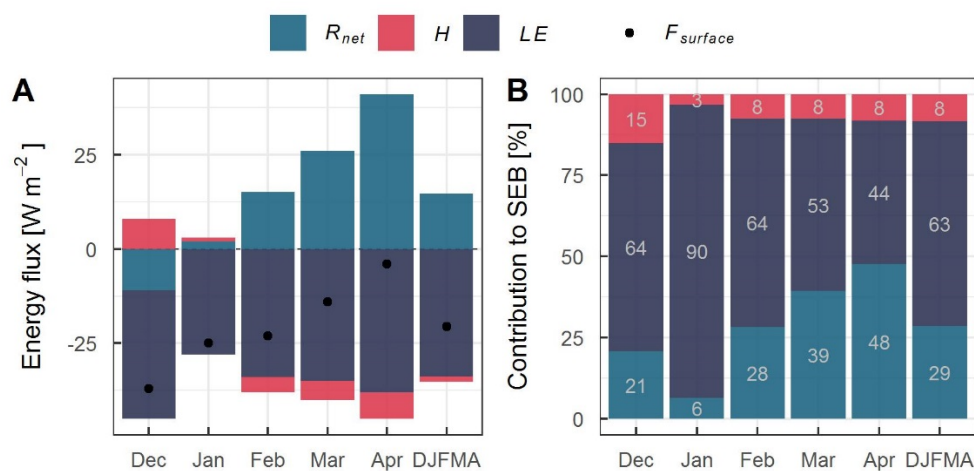
330 **Figure 7. (A) Mean monthly energy flux density of R_{net}, H, LE and $F_{surface}$ for DJFMA, 2009-2020. (B) The monthly proportional contribution of R_{net}, H and LE to SEB. DJFMA is the mean of all months. The proportional contributions were calculated by following the approach of Zhang et al. (2013).**

4.4 Diurnal cycle of the meteorological variables and SEB components

Fig. 8 shows the mean diurnal cycle of meteorological variables and SEB components at the AWS-M. The mean diurnal cycle

335 of T_{air} and T_s was well below 0°C. However, on certain days T_s was above 0°C (6% of the half-hourly data points) but limited

to peak daytime hours between 11:00 and 14:00 IST. Positive T_s was observed when the snowpack was thin about 20 cm or

lower (based on n = 38965 half-hourly SR50A data points between December 2009 and April 2015). RH was the lowest around

late-morning (~10:00) and the highest in the evening at ~18:00. u was maximum during the afternoon (~14:00), which

corresponded well with the steep drop of T_{air} in the afternoon, a typical valley glacier phenomenon (Greuell and Smeets, 2001).

340 S_{in}, S_{out}, L_{in} and L_{out} were the largest at noon when the solar zenith angle was the highest, and the diurnal cycle was opposite

for CF. During the daytime, initially, the energy is absorbed by the skin layers of the snow surface from the balance between

S_{in} and S_{out} (positive S_{net}). S_{net} is compensated by the energy loss through the balance between L_{in} and L_{out} (negative L_{net}). The

energy balance between S_{net} and L_{net}, R_{net} is then used to increase the turbulence of the surface boundary layer resulting in

unstable conditions and negative H and LE (Fig. 8). Turbulent heat flux cycle was opposite to S_{in}, whereas identical to R_{ib}

345 (stability). H was positive across the night, with about 11 W m^{-2}, while it started to sink to negative values for a few hours in

the afternoon when the surface was heated up and again became positive in the evening. The negative values of H were

associated with the unstable condition of the surface boundary layer ($R_{ib} < 0$; T_{air} - $T_s < 0$°C; Fig. 8). Contrary to H, LE was

always negative, slightly less negative in the morning and evening. R_{ib} was mostly positive and small, corresponding to

moderately stable conditions of the surface boundary layer (Fig. 8). R_{ib} was negative for ~8 hours between 9:00 and 16:00 due

350 to the unstable surface boundary layer. R_{net} was negative across the night and early morning, while positive during the daytime

following the S_{in} cycle. The negative R_{net} indicated radiative cooling of the surface at night, while the positive R_{net} suggested

the heat transfer into the snow during the daytime. The $F_{surface}$ was always negative, with slightly lesser negative during the

late afternoon. Despite strong positive R_{net} during the peak-daytime, $F_{surface}$ did not go positive (Fig. 8). This was because

higher $H + LE$ considerably compensated positive R_{net}. There was a strong negative correlation between half-hourly values of

355 R_{net} and $H + LE$ ($r = -0.78$; $p < 0.001$, n = 59131), which supports that R_{net} is responsible for the diurnal cycle of the H and LE.
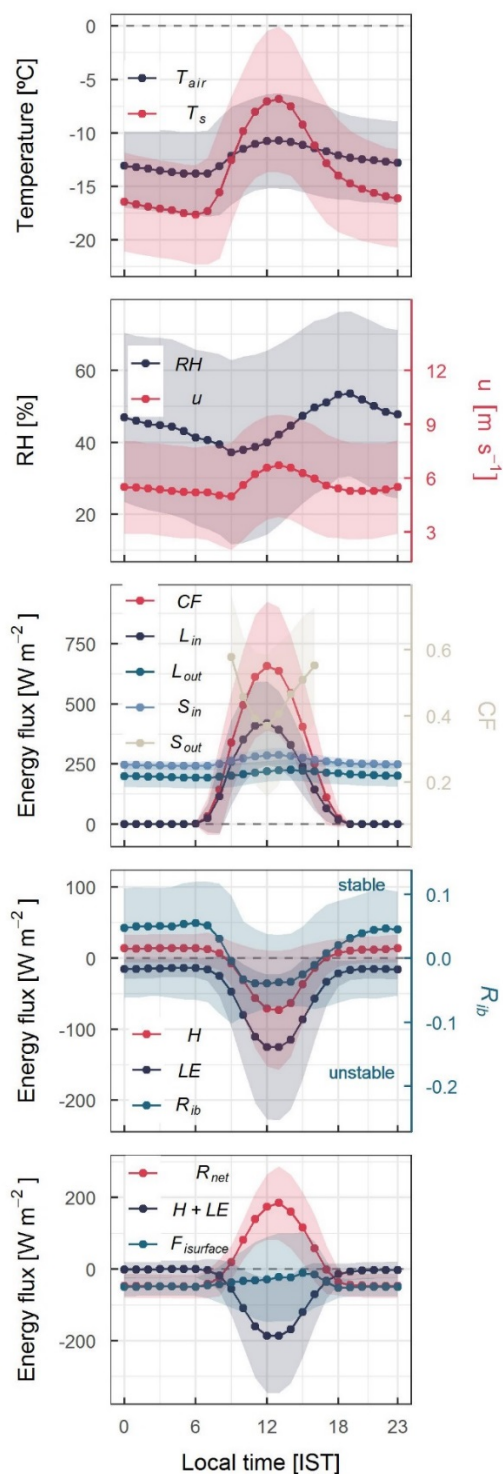
Figure 8. Mean diurnal cycle of meteorological and SEB variables at the AWS-M for DFMFA. Half-hourly data were used between 2009 and 2020. *CF* was calculated between 09:00 and 16:00 IST. Shading is the SD.

4.5 Influence of could cover on SEB components

360 We used *CF* values to differentiate between the clear-sky when $CF \leq 0.2$ and overcast condition when $CF \geq 0.8$, following Chen et al. (2018). Around 24% of the data was categorised as clear-sky, while 10% in the overcast conditions from n = 23903 half-hourly data points (09:00-16:00 IST; 2009-2020; Fig. 9). Overcast condition decreases from January to April with increasing clear-sky conditions.
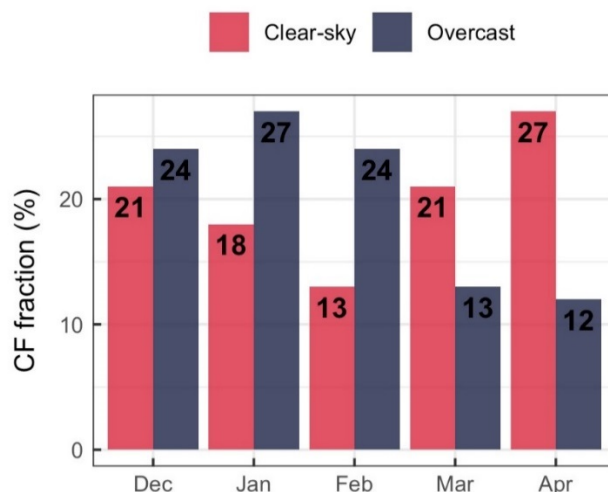
Figure 9. Monthly fraction of clear-sky (*CF* ≤ 0.2) and overcast (*CF* ≥ 0.8) conditions at the AWS-M. Fraction
365 **percentage is calculated from n = 5810 clear-sky and n = 2381 overcast observations from total n = 23903 half-hourly**
**values between 09:00 and 16:00 IST (DJFMA, 2009-2020).**

Fig. 10 shows the daytime half-hourly variation of T_{air}, u, R_{ib} and SEB components. The stability of the surface boundary layer is notable in overcast conditions. Due to comparatively lower T_{air} and higher u in overcast conditions, the surface boundary

370 layer remains near-neutral (R_{ib} close to 0 due to low temperature difference; T_{air} - T_s). Conversely, high negative R_{ib} values (unstable) were observed in clear-sky conditions. All the SEB components were considerably higher in clear-sky than overcast conditions. On average, cloud cover subdued about 70% of the daytime mean S_{in} (744 W m^{-2} in clear-sky to 228 W m^{-2} in overcast conditions). Contrary to S_{in}, cloud cover increased the daytime mean L_{in} by about 25% (201 W m^{-2} in clear-sky to 250 W m^{-2} in overcast conditions).

375 Turbulent heat fluxes were, in general, higher in clear-sky conditions due to higher instability of the surface boundary layer. In clear-sky, the mean daytime H was -66 W m^{-2} which is three-fold than that in overcast conditions (-21 W m^{-2}). Similarly, mean daytime LE was also higher, with -136 W m^{-2} in clear-sky compared to -47 W m^{-2} in overcast conditions. The neutral stability of the surface boundary layer in overcast conditions suppresses the magnitude of H and LE. This is an interconnected process probably in overcast conditions when very high u and cold T_{air} push R_{ib} close to 0, resulting in a reduced magnitude

380 of H and LE (Fig. 10). In clear-sky conditions, more negative LE was due to the surface's intense heating (higher T_{air} - T_s),

which creates a stronger moisture gradient (q - q_s) than the overcast conditions. $F_{surface}$ showed a slight daytime variation in clear-sky but no significant variation in overcast conditions.
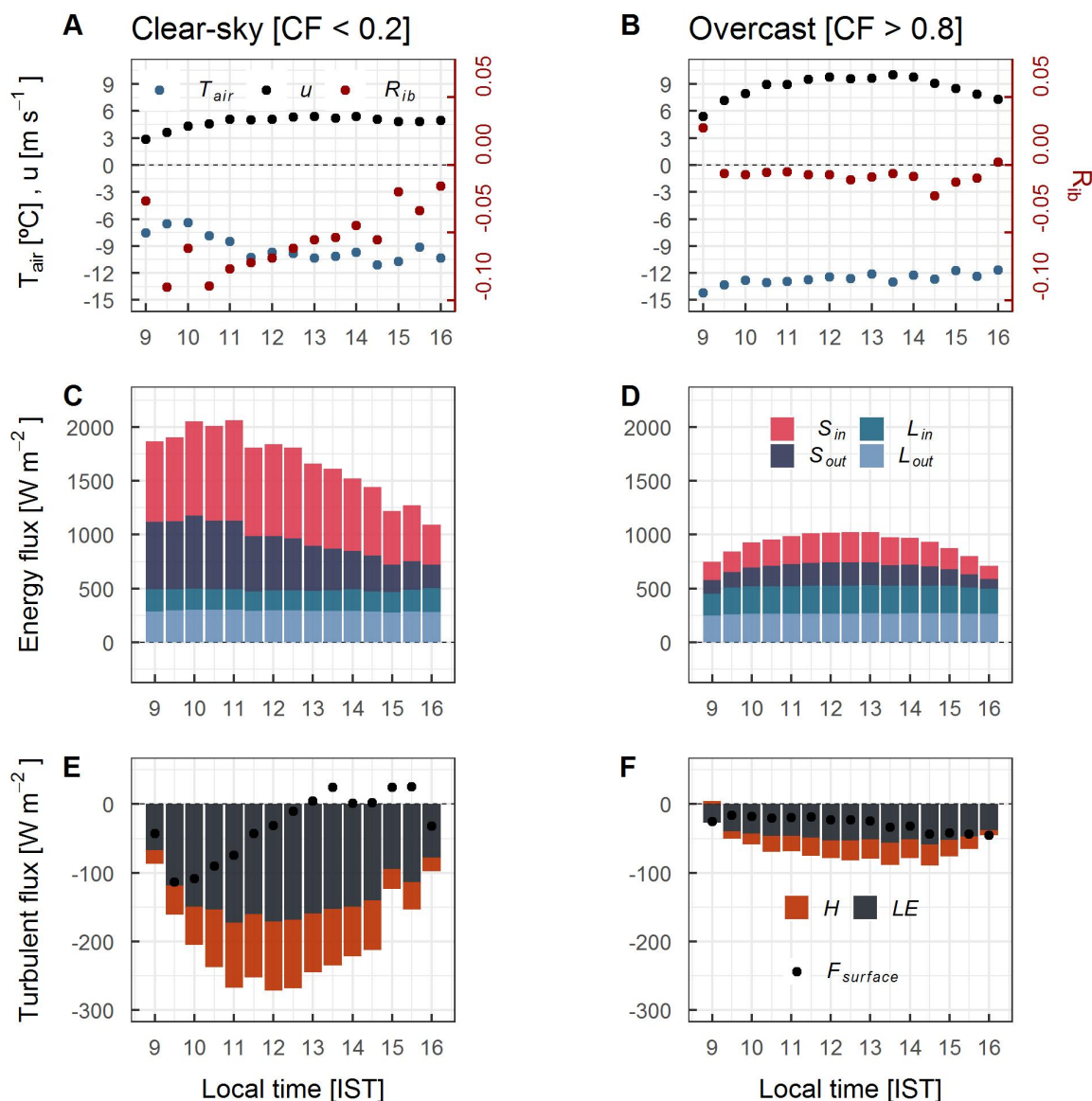

Figure 10. Daytime (09:00-16:00 IST) diurnal cycle of T_{air}, u, R_{ib} and SEB components under the clear-sky ($CF \le 0.2$) and overcast ($CF \ge 0.8$) conditions.

4.6 Turbulent heat fluxes under different cloud conditions

Correlations between half-hourly values of H and LE and meteorological variables were developed (Fig. 11). H was strongly
390   positively correlated with the temperature difference between air and surface (T_{air} - T_s) in clear-sky ($r = 0.96$; $p < 0.001$) and
overcast conditions ($r = 0.83$; $p < 0.001$). That means H increases as the difference in temperature increases (Fig. 12). Similarly,
LE was strongly correlated with T_{air} - T_s in clear-sky ($r = 0.84$; $p < 0.001$) but moderately correlated in overcast conditions ($r = 0.50$; $p < 0.001$). This suggests that the difference in temperature significantly influences the near-surface moisture gradient
in clear-sky conditions, resulting in higher negative LE (Fig. 12). The correlation of H with the specific humidity difference (q
395   - q_s) was moderate in clear-sky ($r = 0.57$; $p < 0.001$) and weak in overcast conditions ($r = 0.10$; $p < 0.001$). Correlation of LE
with q - q_s was strong in clear-sky ($r = 0.82$; $p < 0.001$) as well as overcast conditions ($r = 0.70$; $p < 0.001$). That means LE
increases as the difference in specific humidity increases (Fig. 12). Due to higher near-surface heating and convection, the
near-surface moisture gradient is steeper in clear-sky than in overcast conditions (Fig. 12). There is a clear pattern of more
negative LE with increasing q - q_s (Fig. 12); however, the correlations were not that strong ($r = 0.82$ in clear-sky; $r = 0.70$ in
400   overcast). This could be partly explained by the overestimation of LE in near-neutral conditions ($R_{ib} \approx 0$), which increases the
stability function ($\Phi_{m/h/v}$), resulting in a higher magnitude of LE. The difference in atmospheric stability in clear-sky and
overcast conditions explains the difference in correlations. In this regard, Steiner et al. (2018) discussed that atmospheric
stability correction is crucial to estimate H and LE accurately under different cloud conditions and tricky to handle for a rapidly
changing mountain atmosphere. No strong correlation was observed between H and u in both clear-sky ($r = -0.27$; $p < 0.001$)
405   and overcast conditions ($r = -0.35$; $p < 0.001$). Similarly, LE and u were also not strongly correlated both in clear-sky ($r = -0.37$; $p < 0.001$) and overcast conditions ($r = -0.33$; $p < 0.001$). However, the negative correlation with u suggests that H and
LE increase as sink as u increase and vice versa. The weak correlation of LE with u could be partly explained by the very
strong winds $> \sim 10$ m sec^{-1} at the AWS-M site with high $RH > \sim 70\%$ (Fig. S3), which limits LE magnitude. Such higher winds
were often observed in overcast conditions with precipitation (Fig. S3) and possibly associated with WDs storms. Very strong
410   u keeps the snow surface cool and maintain a reduced T_{air} - T_s and q - q_s, resulting in a reduced LE magnitude (Fig. S4). Overall,
the atmospheric stability of the surface boundary layer —governed by the cloud cover— plays a key role in near-surface
turbulent flux exchange at the AWS-M.
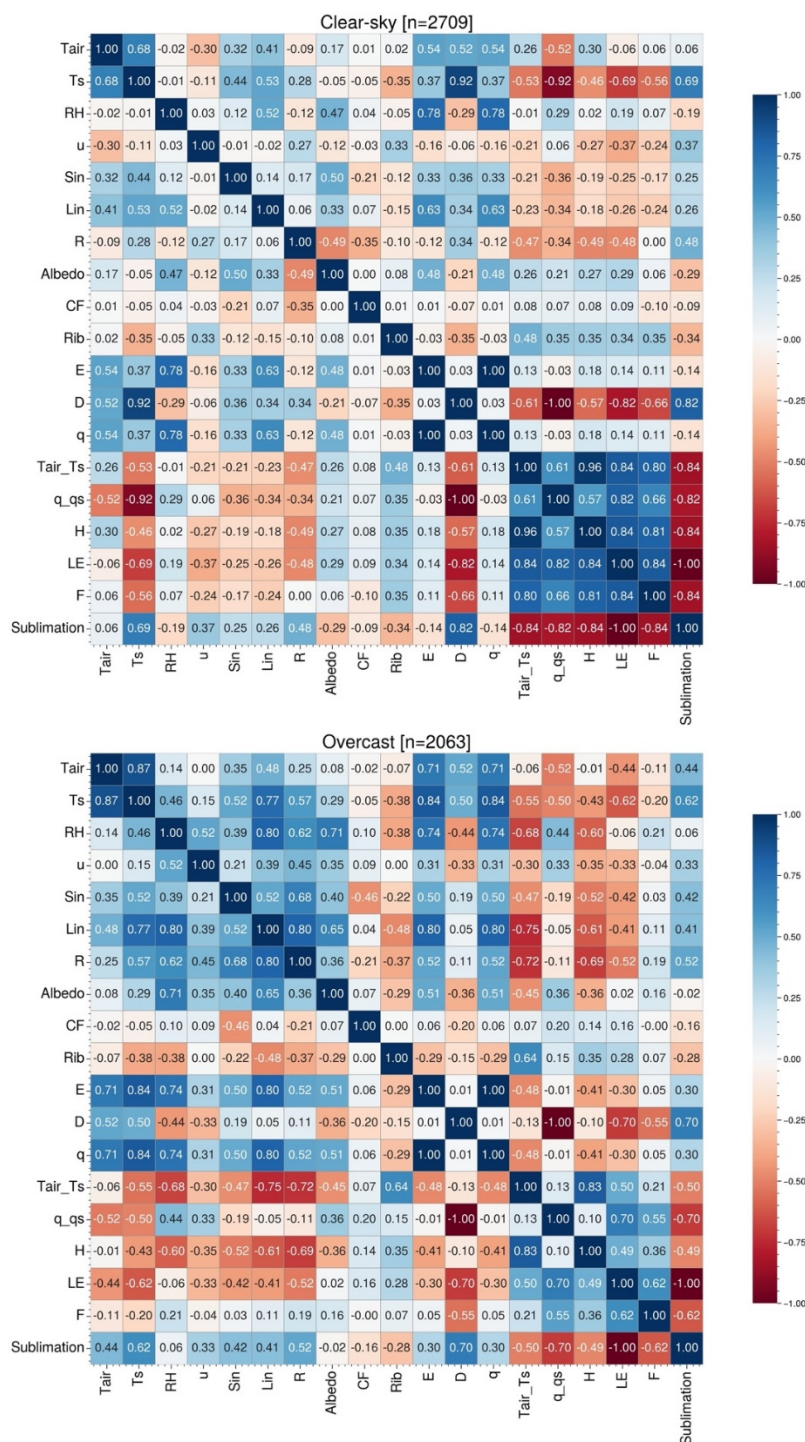
Figure 11. Pearson correlation coefficient (*r*) matrix of various meteorological and SEB components at the AWS-M in clear-sky and overcast conditions between 09:00 and 16:00 IST, 2009-2020. Number (n) of half-hourly data points are shown on top of the panels.
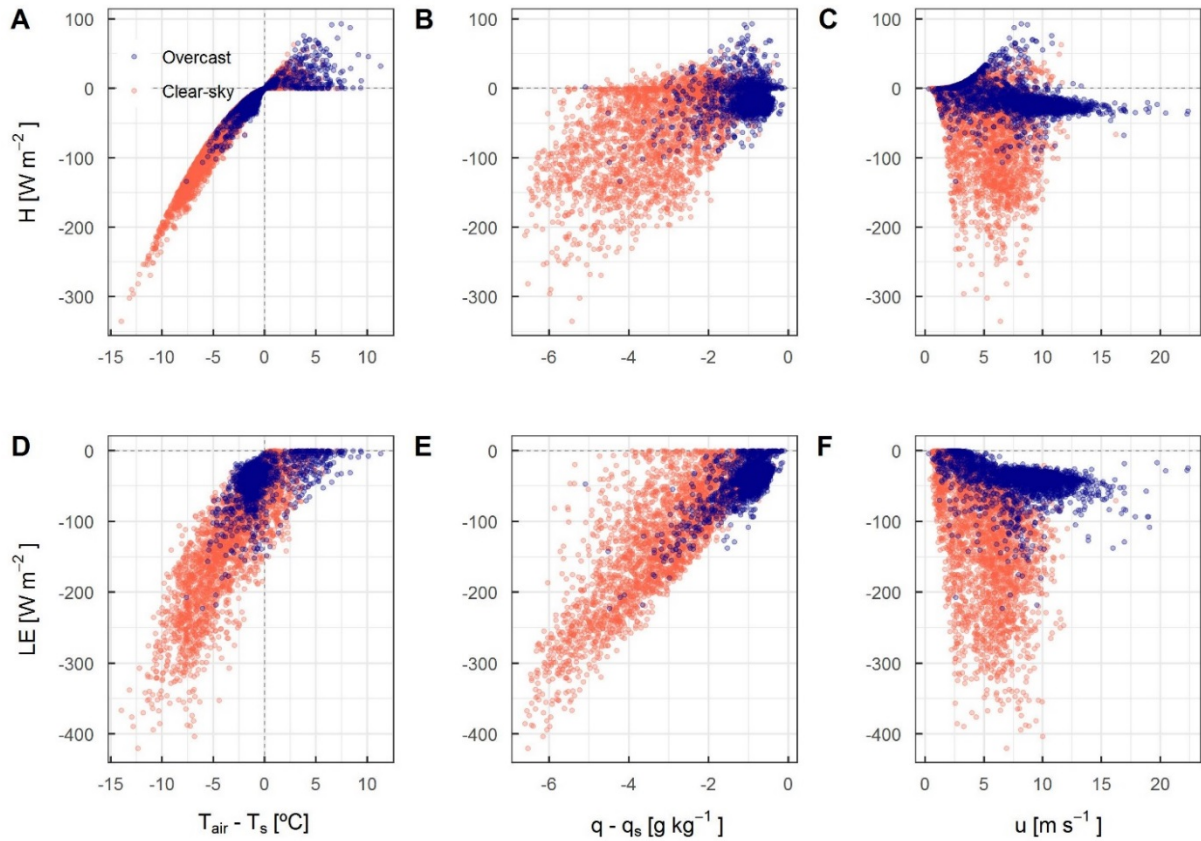
Figure 12. Half-hourly values of the temperature difference (T_{air} - T_s), specific humidity difference (q - q_s) and u compared with H and LE between 09:00 and 16:00 IST for DJFMA, 2009-2020. Red circle represents clear-sky (n = 2709) and blue represents overcast conditions (n = 2063).

4.7 Sublimation

Half-hourly LE fluxes were converted to sublimation following Eq. 8. At the AWS-M site, the mean daily sublimation was 1.1 ± 0.5 mm w.e., corresponding to a cumulative DJFMA mean sublimation loss of 145 ± 25 mm w.e. over 2009-2020 (Table 3). The mean daily sublimation rate was almost three times higher in clear-sky (3.7 ± 2.6 mm w.e.) than in overcast conditions (1.3 ± 0.8 mm w.e.), indicating the role of cloud cover. The mean monthly sublimation was highest in March at 32 ± 7 mm w.e. and lowest in January at 26 ± 7 mm w.e. The yearly cumulative sublimation varied across the study period, from a minimum of 85 mm w.e. in 2009/10 to 172 mm w.e. in 2019/20 (Table 3). Notably, the snowfall amounts were often similar over these years (e.g., 2009/10, 2017/18, 2019/20), suggesting a stronger control of other meteorological variables on sublimation, particularly RH and $T_{s,}$ than snowfall (Table 3). For example, in 2009/10, cumulative sublimation was lowest (85 mm w.e.), which was associated with the lowest T_s (-13.4°C) and the highest frequency of $RH > 80\%$ (8.9%) during the study period (Table 3; Fig. S5). Further, S_{in} was also the lowest in 2009/10 (Table 3). The opposite condition prevailed during 2017/18 and 2019/20 when T_s were considerably warmer at -6.7°C and -7.4°C, respectively, $RH > 80\%$ was the lowest at 3.6%

The Cryosphere
Discussions
Open Access
EGU

and 4.4%, and S_{in} was the highest at 491 and 494 W m^{-2}. This implies that cold and cloudy days restricts sublimation (discussed

more in Sect. 4.7.1).

435

Table 3. Monthly sum of sublimation (S_c; mm w.e.), cumulative sublimation (S_c; mm w.e.), snowfall (mm w.e.) and the fraction of sublimation to snowfall (S_{fra}; %) at the AWS-M during 2009-2020. Snowfall data is based on Geonor and Keylong ('*' marked) precipitation data (see Sect. 3.1). Mean DJFMA meteorology for daytime (08:00 and 16:00 IST) is also shown for corresponding years. $RH > 80\%$ is the frequency of $RH > 80$ in a particular year.

Month	2009/10	2010/11	2011/12	2012/13	2013/14	2014/15	2015/16	2016/17	2017/18	2018/19	2019/20	Mean±SD
December	14	20	30	30	32	49	34	9	39	21	34	28±12
January	11	22	26	37	27	29	31	23	31	22	30	26±7
February	16	27	31	27	38	26	37	35	31	23	38	30±7
March	19	34	42	27	31	27	27	40	36	28	39	32±7
April	25	30	27	29	31	23	29	30	29	27	31	28±3
S_c [mm w.e.]	85	133	156	150	159	153	159	138	167	121	172	145±25
Snowfall [mm w.e.]	485*	474*	415*	850	458*	971	522	613	402	675*	451*	574±187
S_{fra} [%]	18	28	38	18	35	16	30	23	42	18	38	27±10
T_{air} [ºC]	-9.8	-11.2	-12.0	-10.6	-11.6	-10.2	-9.8	-9.5	-9.3	-11.2	-11.1	-10.6±0.9
T_s [ºC]	-13.4	-10.5	-8.5	-8.1	-8.7	-7.7	-7.3	-6.2	-6.7	-10.9	-7.4	-8.7±2.1
u [m s^{-1}]	5.0	5.2	5.9	4.9	5.5	4.7	4.9	5.3	4.8	5.0	4.5	5.0±0.4
RH [%]	41	40	43	39	40	38	36	39	34	41	38	39±3
$RH > 80\%$ [%]	8.9	8.2	5.5	7.5	5.2	7.1	5.0	6.9	3.6	5.8	4.4	6.2±1.7
S_{in} [W m^{-2}]	382	481	462	480	465	476	490	465	491	485	494	470±31

440

4.7.1 Sublimation relationship with meteorological variables

Fig. 13 presents the daytime diurnal cycle of sublimation, u and q for four different meteorological clusters: (1) no filter, (2) high u (> 10 m s^{-1}), (3) high q (> 2 g kg^{-1}) and (4) low q (< 1 g kg^{-1}). We omitted measurements during the night when sublimation is negligible. Sublimation peaks in the early afternoon between 12:00 and 14:00 hours (Fig. 13), soon after the

445 AWS-M site is sunlit. High insolation during the late morning (10:00 - 12:00 IST; Fig. 8) increases the difference in temperature ($T_{air} - T_s$), resulting in relatively stronger convection in the early afternoon, which favours sublimation. Once the snow surface is heated up, the sublimation is conditioned by the vapour pressure deficit (D; Fig. 14). D is the difference between actual vapour pressure at the measurement height and water vapour saturation pressure at the snow surface (Stigter et al., 2018). Low q below 1 g kg^{-1} enhance sublimation (Fig. 13 and 14A). Higher q restricts sublimation because the near-

450 surface atmosphere is saturated; consequently, the water vapour pressure gradient is weak. Sublimation was the largest when T_{air} ranged between -5°C and -10°C and T_s between 0°C and -10°C (Fig. 14B and 14C). This is possibly associated with the

cold storm events, which brings high moisture (Fig. S3) and cold winds in the region (discussed in Sect. 4.6). High R_{net} refers to the clear-sky conditions simultaneously LE is more negative. D show a distinct positive relation with sublimation.

The linear regressions show that D and T_s are the best sublimation predictors for all-data (without CF filter), clear-sky and

455 overcast conditions (Table 4). Linear regressions through D explains 70%, 59% and 49% of the total variance in sublimation for all-data, clear-sky and overcast conditions, respectively, followed by T_s explains 50%, 48% and 39%. Overall, u explain poor variance in sublimation with 0%, 14% and 12% for all-data, clear-sky and overcast conditions, respectively, which disagree with the existing sublimation study (Stigter et al., 2018). They reported that u explains 48% of the total variance in sublimation at the Yala Glacier. The combination (multiple linear regressions) of D, u and T_{air} yields the highest regression

460 R^2. It explains 90%, 94% and 85% of the total variance in sublimation for all-data, clear-sky and overcast conditions, respectively.
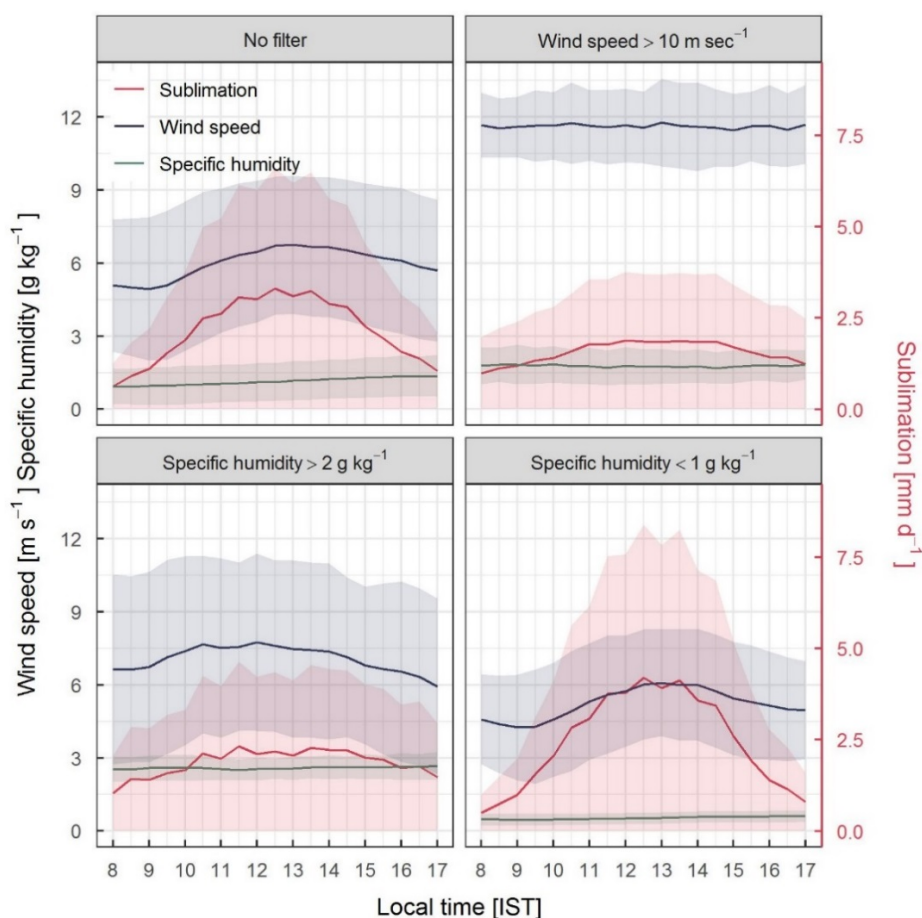
Figure 13. Half-hourly daytime (08:00-17:00) records of sublimation (red), wind speed (blue) and specific humidity (green) at the AWS-M for different clusters: no filter, $u > 10$ m sec^{-1}, $q > 2$ g kg^{-1} and < 1 g kg^{-1}. Data period: DJFMA,

465 **2009-2020. Number of data-points n=30257, 2347, 12295 and 9762 for no filter, $u > 10$ m sec^{-1}, $q > 2$ g kg^{-1} and < 1 g kg^{-1}, respectively.**

The Cryosphere
Discussions

Open Access

EGU
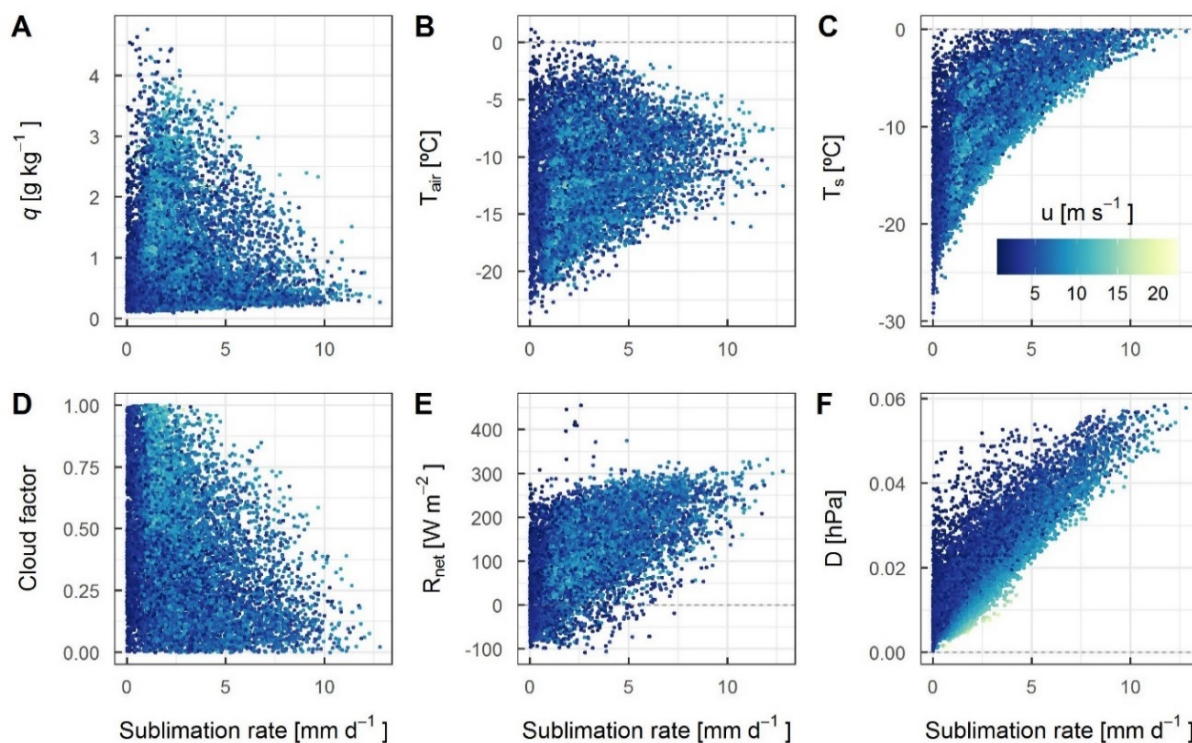
Figure 14. Scatter plot of u, q, T_{air}, T_s, CF, R_{net} and D against sublimation rate at the AWS-M. The colour of the data
points refers to the measured wind speed. Total n = 14088 half-hourly data points between 08:00 and 17:00 IST for
DJFMA (2009-2020).

Table 4. Summary of the k-fold cross-validation (k = 10) linear and multiple linear regression analysis of sublimation
rate and meteorological variables. Total n = 14086, 2708 and 2063 half-hourly data points for all-data, clear-sky and
overcast conditions, respectively, between 08:00 and 17:00 IST for DJFMA (2009-2020). The *p*-value of R^2 is always <
0.001.

Variable	R^2 cross-validation		
	All-data	**Clear-sky**	**Overcast**
D	0.71	0.67	0.49
T_s	0.50	0.48	0.39
R_{net}	0.41	0.24	0.27
S_{in}	0.25	0.06	0.19
CF	0.19	0.01	0.03
T_{air}	0.09	0.01	0.20
q	0.02	0.02	0.10
u	0.00	0.14	0.12
u, D	0.86	0.85	0.85

q, D	0.72	0.69	0.57
q, u	0.03	0.15	0.16
D, u, T_{air}	0.90	0.94	0.85
D, u, T_s	0.86	0.86	0.86
u, q, D	0.86	0.86	0.85
u, q, R_{net}	0.42	0.30	0.28
u, q, S_{in}	0.30	0.23	0.24

5 Discussion

5.1 Factors controlling the latent heat flux

480   LE is crucial in SEB of snow or glacier surface, especially to estimate the surface mass loss through sublimation. We note that LE magnitude is primarily governed by the cloud conditions and the near-surface moisture availability. Cloud cover shapes the prevailing weather at the study site by controlling the stability of the surface boundary layer (Fig. 10). In a stable stratification (T_{air} - T_s > 0°C), snow surface remains cooler than air which restrains LE. It was the opposite in an unstable stratification (T_{air} - T_s < 0°C), which enhanced convection and near-surface turbulence and high negative LE. The low moisture

485   content of the surface creates a steeper negative moisture gradient which favours negative LE (Fig. S4). Stigter et al. (2018) and Guo et al. (2021) noted that u has a direct relationship with LE, which does not agree with the present study. This could be probably due to the frequent influence of partly cloudy conditions across DJFMA (mean DJFMA CF was 0.41; Table 2) with high u (Fig. S3), which maintains a neutral stratification of the boundary layer resulting in a lower LE magnitude. However, the highest multiple regression variance in combination with u (~90%) emphasise the importance of u in controlling

490   LE/sublimation. Fugger et al. (2021) also noted that the relationship between LE and meteorological variables is highly unpredictable, and u fails to explain the variability of LE at five on-glacier sites in the central and eastern Himalaya (see their Fig. A9). Overall, we discerned a greater role of moisture availability in controlling LE magnitude than u. This was also supported by the highest and lowest variance of D and u in sublimation (Table 4).

### 5.2 Sublimation sensitivity to meteorology and roughness and uncertainty sources

495   To test the sensitivity of the calculated sublimation to changes in the input data, we prescribed perturbations of T_{air} (± 1°C), T_s (± 1°C), u (± 10%), RH (± 10%) and z_{0m} (0.0005 m, 0.002 m, 0.003 m and 0.004 m) and re-calculated sublimation for DJFMA, 2009-2020. Similar perturbations for the meteorological variables were applied in the previous studies (Andreassen et al., 2008; Zhang et al., 2013; Steiner et al., 2018; Liu et al., 2021). For z_{0m}, we chose higher and lower order perturbation values considering the high SD of in-situ calculated snow z_{0m} at the AWS-G (0.001 ± 0.003 m; Azam et al., 2014a). Results show that

500   sublimation is most sensitive to z_{0m} and T_s (Fig. 15) because they are the direct drivers of LE. Perturbation of higher order z_{0m} (0.004 m) and +1°C change in T_s increase the mean cumulative sublimation by 21% (30 mm w.e.). For a much lower order z_{0m}

(0.0005 m), the mean cumulative sublimation decreases by 8% (12 mm w.e.). Perturbation to ± 10% change in u yields a ± 8% change in sublimation. The mean cumulative sublimation is roughly three times more sensitive to a ± 1°C change in T_s than a ± 10% change in RH and u.

505   Sublimation sensitivity in this study is similar to that reported for the Lirung Glacier, however, for a debris-covered glacier surface (Steiner et al., 2018). They noted that a ± 1°C change in T_s results in a -42% and 23% change in LE. They also note that LE is less sensitive (± 8%) to a ± 10% change in u. Liu et al. (2021) also reported that LE is considerably less sensitive to change in u and RH (< ± 10% sensitive) than T_s and z_{0m} (> ± 20% sensitive) on the clean-ice East Rongbuk Glacier, Everest region. In general, sublimation is less sensitive to the meteorological variables (T_{air}, RH and u) than z_{0m}. However, it could be
510   higher or significant as the change of ± 1°C in T_{air} or ±10% of RH and u can equally be caused by sensor inaccuracies provided by the sensor manufacturer (Table 1). That means the sensitivity to T_{air}, RH and u could be roughly equal to z_{0m} or T_s. Sensitivities reported in this study have crucial implications in improving the existing hydrological models (Azam and Srivastava, 2020) and distributed SEB models (Patel et al., 2021), where sublimation loss is ignored.

We parameterised the bulk-aerodynamic method without any roughness measurements from the field, which could be a
515   potential uncertainty source of turbulent fluxes. The bulk method was already used in the HK region (Table 5), where the climate setting was similar to that of the Chhota Shigri region, with high wind and dry conditions. We used z_{0m} (0.001 m) which was calculated at the AWS-G site applying a logarithmic profile based on wind speed data from two levels (Azam et al., 2014a), which might have reduced the potential bias from choosing a random z_{0m} or from the existing literature. However, z_{0m} could be higher or lower depending on the snow redistribution at the AWS-M site, which is expected at such a high altitude.
520   Another important uncertainty source of sublimation is blowing snow and erosion (Wagnon et al., 2013), especially over a strong wind-prone site. A wide variation of blowing snow sublimation rates is reported in the literature, depending on the climate and snow blow model setup (Zwaaftink et al., 2013). However, modelling blowing snow sublimation is beyond the scope of this study and might have led to an underestimation of the sublimation in this study. However, considering all the above uncertainties, the mean daily sublimation at the AWS-M site (1.1 mm d^{-1}) agrees well with the eddy-covariance-based
525   sublimation of 1 mm d^{-1} at the Yala Glacier (Stigter et al., 2018), where the reported meteorological condition is identical as at the AWS-M.
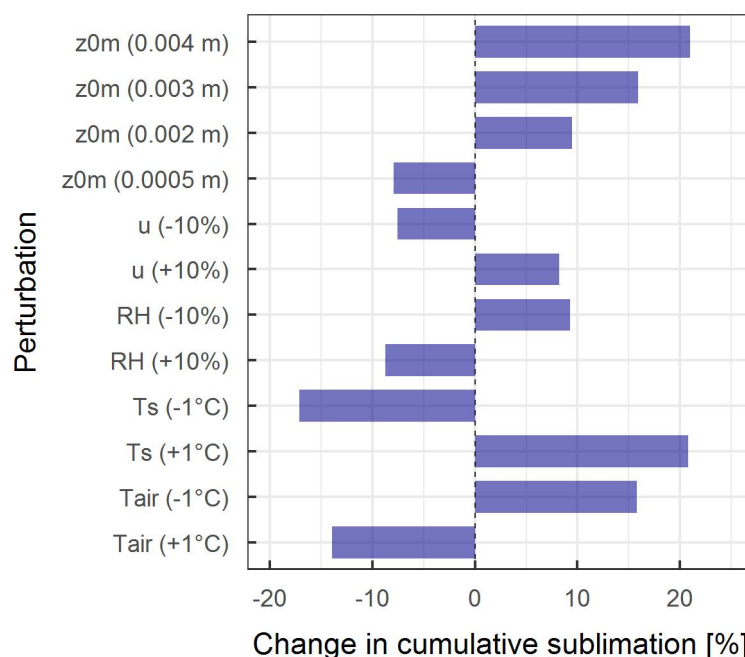
Figure 15. Calculated change in mean cumulative sublimation after applying perturbations to T_{air} (±1°C), T_s (±1°C), u (±10%), RH (±10%), snow z_{0m} (0.0005 m, 0.002 m, 0.003 m and 0.004 m).

5.3 Comparison of sublimation rates with other HK/HMA glaciers

This section discusses the existing sublimation rates/studies across the HMA glaciers/snow-covered sites compared to the Chhota Shigri region (Table 5). The mean daily winter sublimation rate estimated in this study (1.1 ± 0.5 mm d^{-1}) is roughly similar to the mean sublimation (~0.2 to ~2 mm d^{-1}) on the other glacier/snow-covered sites across HMA (Table 5). Sublimation rates during winter were of higher values in the Pamir region, e.g., Muztag Ata No. 1 (Zhu et al., 2018) and Muji site (Zhu et al., 2020) and relatively lower in the inland/central Tibet region, e.g., Qiangtang No. 1 (Li et al., 2018) and Dongkemadi site (Liang et al., 2018). This is likely due to the relatively dry condition in the western parts of HMA than the central or eastern parts (see RH column in Table 5). However, such spatial understanding needs more studies and direct measurements to confirm. The only in-situ lysimeter measured sublimation is available on the East Rongbuk Glacier at ~6500 m a.s.l. (Yang, 2010). Their measured sublimation rate was 1.9 mm d^{-1} during late winter that is similar to the upper limit of our long-term daily sublimation rate. The only eddy-covariance measured sublimation rate during winter at the Yala Glacier was 1 mm d^{-1} which is identical to the sublimation calculated at the AWS-M at the Chhota Shigri moraine. At the Pindari Glacier AWS site (off-glacier; 3750 m a.s.l.), the sublimation rate for a transient snow-cover was estimated to be ~0.3 mm d^{-1} during winter (Singh et al., 2020). Sublimation during the summer-monsoon season, in general, was lower (Table 5), which could be due to the ISM-driven warm and moist atmosphere in the southern slope of the HK region. However, sublimation is higher at very high altitudes despite high summer-monsoon humidity, e.g., East Rongbuk Glacier site (6523 m a.sl.). The high

moisture also impacts Tibetan glaciers, particularly those located in the northern slope of the HK region and central Tibet (Mölg et al., 2012; Li et al., 2018). In the Nepalese central Himalaya, we note a seasonal variation of sublimation as indicated by the higher value of 2.4 and 1.8 mm d⁻¹ in the Yala Glacier during post- and pre-monsoon. Litt et al. (2019) also reported a significantly higher sublimation rate of 7.1 and 1.9 mm d⁻¹ during post- and pre-monsoon on the Mera Glacier when the

550 moisture content is relatively higher than in winter. Higher sublimation characteristics in moist/wet seasons do not agree with the present study, but our observation is limited to the winter season only. However, such higher sublimation can also be partially attributed to snow blowing/redistribution at such high-altitude sites (Barral et al., 2014; Wagnon et al., 2013; Huintjes et al., 2015b). Overall, the favourable climatic conditions at higher altitudes in the western Himalaya and HMA, i.e., dry air, low atmospheric pressure and high wind speed, support sublimation mass loss as observed in this study and previously reported

555 (Matthews et al., 2020; Litt et al., 2019; Stigter et al., 2018; Zhu et al., 2018).

Table 5. Compilation of sublimation rate across the HMA region. '*' refers to the evaporation values.

Site	Altitude (m a.s.l.)	Region	Period of observation	Season approx. to Chhota Shigri	Surface	Method	S (mm d⁻¹)	RH (%)	u (m)	Reference
					Tibetan Plateau					
Zhadang	5665	Nyainqentanglha Shan	1 October to 31 May, 2008-2013	Winter	Glacier-wide	Bulk-aerodynamic	0.5	44	3.6	Zhu et al. (2018)
Muztag Ata No. 15	4400	Eastern Pamir	1 October to 31 May, 2008-2013	Winter	Glacier-wide	Do	2	42	6.4	Zhu et al. (2018)
Parlung	4800	Southeast TP	1 October to 31 May, 2008-2013	Winter	Glacier-wide	Do	0.4	64	3.4	Zhu et al. (2018)
Muji	4685	Northeast Pamir	1 October to 31 May, 2011- 2017	Winter	Glacier-wide	Do	0.5	50	4	Zhu et al. (2020)
Qiangtang No. 1	5882	Inland TP	1 October to 31 May, 2012-2016	Winter	Glacier-wide	Do	0.4	46	6.8	Li et al. (2018)
Guliya Ice Cap	6000	Kunlun Shan	1 October to 31 May, 2015-2016	Winter	Glacier-wide	Do	0.3	67	7.9	Li et al. (2019)
Dongkemadi	5600	Central TP	7 October 1992 to 4 May 1993	Winter	Glacier ELA	Do	0.2		4.3	Liang et al. (2018)
August-one	4817	Qilian Mountains	Jan-May, Oct-Sept, 2016-2020	Winter	Glacier	Do	0.4	68	6.9	Guo et al. (2021)
					Himalaya					
Pindari	3750	Central Himalaya	December 2016 to February 2017	Winter	Medial moraine	Monin-Obukhov theory	~0.3	55	1.2	Singh et al. (2020)
Yala	5350	Central Himalaya	15 October 2015 to 20 April 2017	Winter	Glacier/ablation zone	Eddy-covariance	1	~40	~2.5	Stigter et al. (2018)
Yala	5330	Do	1 October to 15 November, 2012-2017	Post-monsoon	Glacier/ablation zone	Bulk-aerodynamic	2.4	-	-	Litt et al. (2019)
Yala	5330	Do	10 May to 5 June, 2012-2017	Pre-monsoon	Glacier/ablation zone	Do	1.8	-	-	Do
Mera	5360	Do	1 October to 15 November, 2012-2017	Post-monsoon	Glacier/ablation zone	Do	1.9	-	-	Do
Mera	6543	Do	10 May to 5 June, 2012-2017	Pre-monsoon	Glacier/accumulation zone	Do	7.1	-	-	Do
Lirung	4250	Do	26 September to 12 October 2016	Post-monsoon	Glacier debris	Eddy-covariance	1.8-2.8*	~60	~3	Steiner et al. (2018)
South Col, Everest	7945	Do	22 May to 31 October 2019	Summer-monsoon	Ice-rock surface	Bulk-aerodynamic	~0.8	~60	6.3	Matthews et al.(2020)
East Rongbuk	~6500	Do	28 April to 2 May 2008	Pre-monsoon	Glacier	Lysimeter	1.9	-	-	Yang (2010)

East Rongbuk	6523	Do	1 May to 22 July 2005	Summer-monsoon	Glacier	Bulk-aerodynamic	0.05-1.2	60	4.2	Liu et al. (2021)
Xixibangma	5900	Do	23 August to 29 September 1991	Summer-monsoon	Glacier	Calculated	0.02	36	5.9	Aizen et al. (2002)
Naimona'nyi	5543	Do	1 October 2010 to 31 May 2018	Winter	Glacier-wide	Bulk-aerodynamic	0.6	34	5.5	Zhu et al. (2021)
Chhota Shigri	4670	Western Himalaya	1 Dec 2012 to 29 Jan 2013	Winter	Glacier/ablation zone	Do	0.8	44	4.9	Azam et al. (2014a)
Chhota Shigri	4863	Do	1 December to 30 April, 2009-2020	Winter	Seasonal snow on moraine	Do	1.1	43	5	This study

5.4 Sublimation fraction to winter snowfall and its importance

560   Sublimation is a substantial component of the surface mass balance in the HK glaciers (Azam et al., 2021). Wagnon et al. (1999) discussed that sublimation supports the existence of high-altitude glaciers because sublimation limits $F_{surface}$ for melting by counterbalancing it through high negative LE. As the latent heat of sublimation, L_s (2.849×10^6 J kg^{-1}) is 8.5 times the latent heat of fusion (3.34×10^5 J kg^{-1}), the energy consumed by sublimation is 8.5 times higher than that consumed for an equal amount of melting (Liu et al., 2021). Hence, sublimation can substantially decrease the energy supply for glacier melting.

565   The cumulative sublimation at the AWS-M ranges from 85 mm w.e. to 172 mm w.e. with a long-term mean of 145 ± 25 mm w.e. for DJFMA during 2009-2020 (Table 3). The cumulative snowfall ranges from 402 mm to 971 mm, with a mean of 574 ± 187 recorded at the glacier base camp and Keylong station (reliability of Keylong precipitation is discussed in Sect. 3.1) for DJFMA during 2009-2020 (Table 3). The cumulative sublimation loss accounts for 16-42% of the fraction of winter snowfall at the AWS-M site (Table 3). This mass loss is substantial compared to other parts of the HK region. For example, in the

570   central Himalaya at the Yala Glacier, sublimation loss was 21% of the snowfall during one winter season (Stigter et al., 2018). Similarly, sublimation loss was about 14-18% of the total snowfall in the Pheriche sub-catchment of the Dudh Koshi basin in Nepal, based on distributed glaciohydrological model (Mimeau et al., 2019). Based on satellite-derived datasets, Gascoin (2021) showed that the sublimation ratio to snowfall can exceed 60% in the high-altitude areas in the north-western part of the Himalaya, e.g., Ladakh and Karakoram. In the Chinese Altai Mountain at the Irtysh River basin, sublimation accounts for 19%

575   of the snowfall estimated through a physically based snow model (Wu et al., 2021). In the Tibetan Plateau, at the Zhadang Glacier, sublimation loss was 26% of the total mass loss annually (Huintjes et al., 2015a). At the August-one Glacier in the Qilian Mountains, evapo-sublimation accounts for 15% of the annual precipitation, with the most during winter periods (Guo et al., 2021). At the Qiangtang No 1 Glacier, the sublimation and evaporation loss fraction was about 65-169% of the snowfall during 2012-2016, which is a significantly higher mass loss than gain (Li et al., 2018). Such a higher sublimation fraction over

580   non-melt seasons was associated with high wind speed (~7 m sec^{-1}), lower RH (~46%) and low annual precipitation (362-614 mm). This endorse that the dry and windy environment supports sublimation in the HK region.

Sublimation is the largest mass loss component during winter. Nonetheless, the sum of winter snowfall may have significant uncertainties considering the under-catch of solid precipitation (Collier and Immerzeel, 2015; Shea et al., 2015; Doblas-Reyes et al., 2021) by the Geonor gauge at the glacier base camp and Keylong station due to strong wind. For example, the snowfall

585 catch efficiency of a Geonor T-200B equipped with a single-Alter windshield (the one functional at the glacier base camp) could be about 50% or less at a wind speed of about 5 m s^{-1} or higher (Wolff et al., 2015; see their Fig. 5). Despite the uncertainty in winter snowfall, our results indicate that sublimation loss during DJFMA is a significant component of winter mass distribution. Therefore, it is crucial to include sublimation in future surface mass balance and hydrological modelling in the region.

590

6 Conclusions and perspectives

In this study, we presented an 11-year record of observed meteorology, SEB and sublimation for DJFMA at 4863 m a.s.l. on the Chhota Shigri Glacier moraine in the western Himalaya. We investigated the role of turbulent heat fluxes in SEB, the influence of cloud cover and the sublimation and its importance in winter mass distribution during 2009-2020.

595 The net short-wave radiation was the primary energy source of SEB. At the same time, turbulent heat fluxes ($H + LE$) significantly sink the energy, resulting in negative residual energy ($F_{surface}$) at the surface throughout DJFMA. Although net short-wave radiation was the largest contributor in SEB across the HMA, we found a significant role of latent heat flux, contributing > 60% during the winter months. The moisture availability primarily controls the magnitude of latent heat flux with considerable influence from snow surface temperature and wind speed. Interestingly, we found that the strong and cold

600 winds, probably from the WDs storms, acts as an impeder of latent heat flux at the AWS-M site by setting up high moisture and cold temperature regime.

The large variability in SEB components was directly related to cloud cover, which primarily affects incoming short-wave radiation (restraints by 70%) and incoming long-wave radiation (raises by 25%). The cloud cover also influences turbulent heat fluxes by restraining them above 50%. The mean daily sublimation at the AWS-M was about three times lower on cloudy

605 days than clear-sky days due to the low incoming short-wave radiation. The mean daily sublimation was similar to the sublimation rates of other HK and HMA glaciers during winter. The vapour pressure deficit, along with surface temperature and wind speed were emerged to be the best predictors of sublimation based on the linear regression analysis. A sensitivity analysis showed that sublimation is most sensitive to the changes in z_{0m} and T_s suggesting its cruciality for accurate SEB and sublimation.

610 The cumulative DJFMA sublimation was about 16-42% of the fraction of winter snowfall at the AWS-M site, which is higher than other observations across the HK and HMA. Hence, sublimation is one of the significant mass balance components during the winter, especially in a dry-cold-windy environment. However, sublimation estimates and winter snowfall could be significantly uncertain in the high-mountain sites, considering their sensitivity to meteorological forcing, surface roughness length, sensor inaccuracies and calculation errors; thus, it requires more detailed studies.

615 Given the limitations, this 11-year dataset demonstrates how glacier-based studies can improve our understanding of local-scale meteorological factors affecting SEB and sublimation in the HK region. This study underscores the need for extensive measurements of high-quality on-glacier weather data using the eddy-covariance technique and snowfall for robust region-wide modelling.

Code Availability

620 Codes for SEB analysis will be made online through open access repository.

Supplementary Material

The supplement related to this article is available in the discussion page.

Author Contribution

625 AM, TA, MFA and PW conceptualised the study. ALR supervised the study. AM performed the analysis, developed the figures and wrote the paper. MS helped in SEB calculations. CS partly compiled the existing sublimation studies across the HMA. All authors contributed significantly to preparing the draft manuscript and discussion and supported the data analysis.

Competing Interests

The authors declare that they have no conflict of interest.

Acknowledgements

630

640

The Cryosphere
Discussions

References

Acharya, A. and Kayastha, R. B.: Mass and Energy Balance Estimation of Yala Glacier (2011–2017), Langtang Valley, Nepal, Water, 11, 6, https://doi.org/10.3390/w11010006, 2019.

Aizen, V. B., Aizen, E. M., and Nikitin, S. A.: Glacier regime on the northern slope of the Himalaya (Xixibangma glaciers), Quaternary International, 97–98, 27–39, https://doi.org/10.1016/S1040-6182(02)00049-6, 2002.

Andreassen, L. M., Broeke, M. R. V. D., Giesen, R. H., and Oerlemans, J.: A 5 year record of surface energy and mass balance from the ablation zone of Storbreen, Norway, J. Glaciol., 54, 245–258, https://doi.org/10.3189/002214308784886199, 2008.

Azam, M. F., Wagnon, P., Vincent, C., Ramanathan, Al., Favier, V., Mandal, A., and Pottakkal, J. G.: Processes governing the mass balance of Chhota Shigri Glacier (western Himalaya, India) assessed by point-scale surface energy balance measurements, The Cryosphere, 8, 2195–2217, https://doi.org/10.5194/tc-8-2195-2014, 2014a.

Azam, M. F., Wagnon, P., Vincent, C., Ramanathan, A., Linda, A., and Singh, V. B.: Reconstruction of the annual mass balance of Chhota Shigri glacier, Western Himalaya, India, since 1969, Ann. Glaciol., 55, 69–80, https://doi.org/10.3189/2014AoG66A104, 2014b.

Azam, M. F., Ramanathan, A., Wagnon, P., Vincent, C., Linda, A., Berthier, E., Sharma, P., Mandal, A., Angchuk, T., Singh, V. B., and Pottakkal, J. G.: Meteorological conditions, seasonal and annual mass balances of Chhota Shigri Glacier, western Himalaya, India, Ann. Glaciol., 57, 328–338, https://doi.org/10.3189/2016AoG71A570, 2016.

Azam, M. F., Wagnon, P., Berthier, E., Vincent, C., Fujita, K., and Kargel, J. S.: Review of the status and mass changes of Himalayan-Karakoram glaciers, J. Glaciol., 1–14, https://doi.org/10.1017/jog.2017.86, 2018.

Azam, M. F., Kargel, J. S., Shea, J. M., Nepal, S., Haritashya, U. K., Srivastava, S., Maussion, F., Qazi, N., Chevallier, P., Dimri, A. P., Kulkarni, A. V., Cogley, J. G., and Bahuguna, I. M.: Glaciohydrology of the Himalaya-Karakoram, Science, https://doi.org/10.1126/science.abf3668, 2021.

Azam, Mohd. F. and Srivastava, S.: Mass balance and runoff modelling of partially debris-covered Dokriani Glacier in monsoon-dominated Himalaya using ERA5 data since 1979, Journal of Hydrology, 590, 125432, https://doi.org/10.1016/j.jhydrol.2020.125432, 2020.

Barral, H., Genthon, C., Trouvilliez, A., Brun, C., and Amory, C.: Blowing snow in coastal Adélie Land, Antarctica: three atmospheric-moisture issues, The Cryosphere, 8, 1905–1919, https://doi.org/10.5194/tc-8-1905-2014, 2014.

Bintanja, R.: The local surface energy balance of the Ecology Glacier, King George Island, Antarctica: measurements and modelling, Antarctic Science, 7, 315–325, https://doi.org/10.1017/S0954102095000435, 1995.

Bookhagen, B. and Burbank, D. W.: Toward a complete Himalayan hydrological budget: Spatiotemporal distribution of snowmelt and rainfall and their impact on river discharge, Journal of Geophysical Research: Earth Surface, 115, https://doi.org/10.1029/2009JF001426, 2010.

Brutsaert, B.: Evaporation in the Atmosphere: Theory, History and Application, Kluwer Acad., Norwell, Mass, 299 pp., 1982.

Chambers, J. R., Smith, M. W., Quincey, D. J., Carrivick, J. L., Ross, A. N., and James, M. R.: Glacial Aerodynamic Roughness
675   Estimates: Uncertainty, Sensitivity, and Precision in Field Measurements, J. Geophys. Res. Earth Surf., 125,
         https://doi.org/10.1029/2019JF005167, 2020.

Chen, J., Qin, X., Kang, S., Du, W., Sun, W., and Liu, Y.: Effects of clouds on surface melting of Laohugou glacier No. 12,
         western Qilian Mountains, China, J. Glaciol., 1–11, https://doi.org/10.1017/jog.2017.82, 2018.

Collier, E. and Immerzeel, W. W.: High-resolution modeling of atmospheric dynamics in the Nepalese Himalaya, The
680   Cryosphere, 120, 9882–9896, https://doi.org/10.1002/2015JD023266, 2015.

Conway, J. P. and Cullen, N. J.: Cloud effects on surface energy and mass balance in the ablation area of Brewster Glacier,
         New Zealand, The Cryosphere, 10, 313–328, https://doi.org/10.5194/tc-10-313-2016, 2016.

Cuffey, K. M. and Paterson, W. S. B.: The physics of glaciers. Fourth edition. Oxford, Butterworth-Heinemann, 2010.

Denby, B. and Greuell, W.: The use of bulk and profile methods for determining surface heat fluxes in the presence of glacier
685   winds, J. Glaciol., 46, 445–452, https://doi.org/10.3189/172756500781833124, 2000.

Doblas-Reyes, F. J,. A. A. Sörensson, M. Almazroui, A. Dosio, W. J. Gutowski, R. Haarsma, R. Hamdi, B. Hewitson, W-T.
         Kwon, B. L. Lamptey, D. Maraun, T. S. Stephenson, I. Takayabu, L. Terray, A. Turner, Z. Zuo, 2021, Linking Global
         to Regional Climate Change. In: Climate Change 2021.: The Physical Science Basis. Contribution of Working Group
         I to the Sixth Assessment Report of the Intergovernmental Panel on Climate Change [Masson-Delmotte, V., P. Zhai,
690   A. Pirani, S. L. Connors, C. Péan, S. Berger, N. Caud, Y. Chen, L. Goldfarb, M. I. Gomis, M. Huang, K. Leitzell, E.
         Lonnoy, J.B.R. Matthews, T. K. Maycock, T. Waterfield, O. Yelekçi, R. Yu and B. Zhou (eds.)]. Cambridge
         University Press. In Press.

Favier, V., Wagnon, P., Chazarin, J.-P., Maisincho, L., and Coudrain, A.: One-year measurements of surface heat budget on
         the ablation zone of Antizana Glacier 15, Ecuadorian Andes, Journal of Geophysical Research: Atmospheres, 109,
695   https://doi.org/10.1029/2003JD004359, 2004.

Favier, V., Agosta, C., Genthon, C., Arnaud, L., Trouvillez, A., and Gallée, H.: Modeling the mass and surface heat budgets
         in a coastal blue ice area of Adelie Land, Antarctica, Journal of Geophysical Research: Earth Surface, 116,
         https://doi.org/10.1029/2010JF001939, 2011.

Fugger, S., Fyffe, C. L., Fatichi, S., Miles, E., McCarthy, M., Shaw, T. E., Ding, B., Yang, W., Wagnon, P., Immerzeel, W.,
700   Liu, Q., and Pellicciotti, F.: Understanding monsoon controls on the energy and mass balance of Himalayan glaciers,
         The Cryosphere Discussions, 1–46, https://doi.org/10.5194/tc-2021-97, 2021.

Gascoin, S.: Snowmelt and Snow Sublimation in the Indus Basin, Water, 13, 2621, https://doi.org/10.3390/w13192621, 2021.

Giesen, R. H. and Andreassen, L. M.: Comparison of the meteorology and surface energy balance at Storbreen and
         Midtdalsbreen, two glaciers in southern Norway, The Cryosphere, 18, 2009.

705 Greuell, W. and Smeets, P.: Variations with elevation in the surface energy balance on the Pasterze (Austria), Journal of
         Geophysical Research: Atmospheres, 106, 31717–31727, https://doi.org/10.1029/2001JD900127, 2001.

The Cryosphere
Discussions

Open Access

EGU

Guo, S., Chen, R., Han, C., Liu, J., Wang, X., and Liu, G.: Five-year analysis of evaposublimation characteristics and its role on surface energy balance SEB on a midlatitude continental glacier, Earth and Space Science, https://doi.org/10.1029/2021EA001901, 2021.

710 Hock, R.: Glacier melt: a review of processes and their modelling, Progress in Physical Geography: Earth and Environment, 29, 362–391, https://doi.org/10.1191/0309133305pp453ra, 2005.

Huintjes, E., Sauter, T., Schröter, B., Maussion, F., Yang, W., Kropáček, J., Buchroithner, M., Scherer, D., Kang, S., and Schneider, C.: Evaluation of a Coupled Snow and Energy Balance Model for Zhadang Glacier, Tibetan Plateau, Using Glaciological Measurements and Time-Lapse Photography, Arctic, Antarctic, and Alpine Research, 47, 573–590,

715 https://doi.org/10.1657/AAAR0014-073, 2015a.

Huintjes, E., Neckel, N., Hochschild, V., and Schneider, C.: Surface energy and mass balance at Purogangri ice cap, central Tibetan Plateau, 2001–2011, J. Glaciol., 61, 1048–1060, https://doi.org/10.3189/2015JoG15J056, 2015b.

IPCC.: IPCC Special Report on the Ocean and Cryosphere in a Changing Climate [H.-O. Pörtner, D.C. Roberts, V. Masson-Delmotte, P. Zhai, M. Tignor, E. Poloczanska, K. Mintenbeck, A. Alegría, M. Nicolai, A. Okem, J. Petzold, B. Rama,

720 N.M. Weyer (eds.)]. In press, 2019.

Iqbal, M.: An introduction to solar radiation, Academic Press, New York, 1983.

Kayastha, R. B., Ohata, T., and Ageta, Y.: Application of a mass-balance model to a Himalayan glacier, J. Glaciol., 45, 559–567, https://doi.org/10.3189/S002214300000143X, 1999.

Kirkham, J. D., Koch, I., Saloranta, T. M., Litt, M., Stigter, E. E., Møen, K., Thapa, A., Melvold, K., and Immerzeel, W. W.:

725 Near Real-Time Measurement of Snow Water Equivalent in the Nepal Himalayas, Front. Earth Sci., 7, https://doi.org/10.3389/feart.2019.00177, 2019.

Kochendorfer, J., Nitu, R., Wolff, M., Mekis, E., Rasmussen, R., Baker, B., Earle, M. E., Reverdin, A., Wong, K., Smith, C. D., Yang, D., Roulet, Y.-A., Buisan, S., Laine, T., Lee, G., Aceituno, J. L. C., Alastrué, J., Isaksen, K., Meyers, T., Brækkan, R., Landolt, S., Jachcik, A., and Poikonen, A.: Analysis of single-Alter-shielded and unshielded

730 measurements of mixed and solid precipitation from WMO-SPICE, Hydrology and Earth System Sciences, 21, 3525–3542, https://doi.org/10.5194/hess-21-3525-2017, 2017.

de Kok, R. J., Steiner, J. F., Litt, M., Wagnon, P., Koch, I., Azam, M. F., and Immerzeel, W. W.: Measurements, models and drivers of incoming longwave radiation in the Himalaya, International Journal of Climatology, 0, https://doi.org/10.1002/joc.6249, 2019.

735 Kuhn, Max.: caret: Classification and Regression Training. R package version 6.0-88. https://CRAN.R-project.org/package=caret, 2021.

Kumar, P., Saharwardi, Md. S., Banerjee, A., Azam, Mohd. F., Dubey, A. K., and Murtugudde, R.: Snowfall Variability Dictates Glacier Mass Balance Variability in Himalaya-Karakoram, Sci Rep, 9, 18192, https://doi.org/10.1038/s41598-019-54553-9, 2019.

740   Li, S., Yao, T., Yang, W., Yu, W., and Zhu, M.: Glacier Energy and Mass Balance in the Inland Tibetan Plateau: Seasonal and
           Interannual Variability in Relation to Atmospheric Changes, Journal of Geophysical Research: Atmospheres, 123,
           6390–6409, https://doi.org/10.1029/2017JD028120, 2018.

       Li, S., Yao, T., Yu, W., Yang, W., and Zhu, M.: Energy and mass balance characteristics of the Guliya ice cap in the West
           Kunlun Mountains, Tibetan Plateau, Cold Regions Science and Technology, 159, 71–85,
745   https://doi.org/10.1016/j.coldregions.2018.12.001, 2019.

       Liang, L., Cuo, L., and Liu, Q.: The energy and mass balance of a continental glacier: Dongkemadi Glacier in central Tibetan
           Plateau, Sci Rep, 8, 12788, https://doi.org/10.1038/s41598-018-31228-5, 2018.

       Litt, M., Shea, J., Wagnon, P., Steiner, J., Koch, I., Stigter, E., and Immerzeel, W.: Glacier ablation and temperature indexed
           melt models in the Nepalese Himalaya, Sci Rep, 9, 5264, https://doi.org/10.1038/s41598-019-41657-5, 2019.

750   Liu, W., Zhang, D., Qin, X., Broeke, M. R. van den, Jiang, Y., Yang, D., and Ding, M.: Monsoon Clouds Control the Summer
           Surface Energy Balance on East Rongbuk glacier (6523 m above sea level), the northern of Mt. Qomolangma
           (Everest), Journal of Geophysical Research: Atmospheres, https://doi.org/10.1029/2020JD033998, 2021.

       Mandal, A., Ramanathan, A., Azam, M. F., Angchuk, T., Soheb, M., Kumar, N., Pottakkal, J. G., Vatsal, S., Mishra, S., and
           Singh, V. B.: Understanding the interrelationships among mass balance, meteorology, discharge and surface velocity
755   on Chhota Shigri Glacier over 2002–2019 using in situ measurements, J. Glaciol., 1–15,
           https://doi.org/10.1017/jog.2020.42, 2020.

       Matthews, T., Perry, L. B., Koch, I., Aryal, D., Khadka, A., Shrestha, D., Abernathy, K., Elmore, A. C., Seimon, A., Tait, A.,
           Elvin, S., Tuladhar, S., Baidya, S. K., Potocki, M., Birkel, S. D., Kang, S., Sherpa, T. C., Gajurel, A., and Mayewski,
           P. A.: Going to Extremes: Installing the World's Highest Weather Stations on Mount Everest, Bull. Amer. Meteor.
760   Soc., https://doi.org/10.1175/BAMS-D-19-0198.1, 2020.

       Mimeau, L., Esteves, M., Zin, I., Jacobi, H.-W., Brun, F., Wagnon, P., Koirala, D., and Arnaud, Y.: Quantification of different
           flow components in a high-altitude glacierized catchment (Dudh Koshi, Himalaya): some cryospheric-related issues,
           23, 3969–3996, https://doi.org/10.5194/hess-23-3969-2019, 2019.

       Mölg, T., Maussion, F., Yang, W., and Scherer, D.: The footprint of Asian monsoon dynamics in the mass and energy balance
765   of a Tibetan glacier, The Cryosphere, 6, 1445–1461, https://doi.org/10.5194/tc-6-1445-2012, 2012.

       Moore, R.: On the use of bulk aerodynamic formulae over melting snow, Nord. Hydrol., 14, 193–206, 1983.

       Nicholson, L. and Stiperski, I.: Comparison of turbulent structures and energy fluxes over exposed and debris-covered glacier
           ice, J. Glaciol., 66, 543–555, https://doi.org/10.1017/jog.2020.23, 2020.

       Nicholson, L. I., Prinz, R., Mölg, T., and Kaser, G.: Micrometeorological conditions and surface mass and energy fluxes on
770   Lewis Glacier, Mt Kenya, in relation to other tropical glaciers, The Cryosphere, 7, 1205–1225,
           https://doi.org/10.5194/tc-7-1205-2013, 2013.

       Oerlemans, J.: Analysis of a 3 year meteorological record from the ablation zone of Morteratschgletscher, Switzerland: energy
           and mass balance, J. Glaciol., 46, 571–579, https://doi.org/10.3189/172756500781832657, 2000.

Oerlemans, J.: Glaciers and Climate Change, CRC Press, 168 pp., 2001.

775   Oke, T. R.: Boundary Layer Climates, 2nd Edn., Routledge, 423 pp., 1987

Patel, A., Goswami, A., Dharpure, J. K., Thamban, M., Sharma, P., Kulkarni, A. V., and Oulkar, S.: Estimation of mass and energy balance of glaciers using a distributed energy balance model over the Chandra river basin (Western Himalaya), Hydrological Processes, https://doi.org/10.1002/hyp.14058, 2021.

R Core Team.: R: A language and environment for statistical computing. R Foundation for Statistical Computing, Vienna,
780   Austria. URL https://www.R-project.org/, 2021.

Radić, V., Menounos, B., Shea, J., Fitzpatrick, N., Tessema, M. A., and Déry, S. J.: Evaluation of different methods to model near-surface turbulent fluxes for a mountain glacier in the Cariboo Mountains, BC, Canada, The Cryosphere, 11, 2897–2918, https://doi.org/10.5194/tc-11-2897-2017, 2017.

Reid, T. D. and Brock, B. W.: An energy-balance model for debris-covered glaciers including heat conduction through the
785   debris layer, J. Glaciol., 56, 903–916, https://doi.org/10.3189/002214310794457218, 2010.

Rounce, D. R., Quincey, D. J., and McKinney, D. C.: Debris-covered glacier energy balance model for Imja–Lhotse Shar Glacier in the Everest region of Nepal, The Cryosphere, 9, 2295–2310, https://doi.org/10.5194/tc-9-2295-2015, 2015.

Schaefer, M., Fonseca-Gallardo, D., Farías-Barahona, D., and Casassa, G.: Surface energy fluxes on Chilean glaciers: measurements and models, The Cryosphere, 14, 2545–2565, https://doi.org/10.5194/tc-14-2545-2020, 2020.

790   Sexstone, G. A., Clow, D. W., Stannard, D. I., and Fassnacht, S. R.: Comparison of methods for quantifying surface sublimation over seasonally snow-covered terrain, Hydrological Processes, 30, 3373–3389, https://doi.org/10.1002/hyp.10864, 2016.

Shea, J. M., Wagnon, P., Immerzeel, W. W., Biron, R., Brun, F., and Pellicciotti, F.: A comparative high-altitude meteorological analysis from three catchments in the Nepalese Himalaya, 31, 174–200,
795   https://doi.org/10.1080/07900627.2015.1020417, 2015.

Singh, N., Singhal, M., Chhikara, S., Karakoti, I., Chauhan, P., and Dobhal, D. P.: Radiation and energy balance dynamics over a rapidly receding glacier in the central Himalaya, International Journal of Climatology, 40, 400–420, https://doi.org/10.1002/joc.6218, 2020.

Slater, T., Lawrence, I. R., Otosaka, I. N., Shepherd, A., Gourmelen, N., Jakob, L., Tepes, P., and Gilbert, L.: Review Article:
800   Earth's ice imbalance, The Cryosphere, 1–21, https://doi.org/10.5194/tc-2020-232, 2020.

Smith, T., Smith, M. W., Chambers, J. R., Sailer, R., Nicholson, L., Mertes, J., Quincey, D. J., Carrivick, J. L., and Stiperski, I.: A scale-dependent model to represent changing aerodynamic roughness of ablating glacier ice based on repeat topographic surveys, J. Glaciol., 1–15, https://doi.org/10.1017/jog.2020.56, 2020.

Steiner, J. F., Litt, M., Stigter, E. E., Shea, J., Bierkens, M. F. P., and Immerzeel, W. W.: The Importance of Turbulent Fluxes
805   in the Surface Energy Balance of a Debris-Covered Glacier in the Himalayas, Front. Earth Sci., 6, https://doi.org/10.3389/feart.2018.00144, 2018.

The Cryosphere
Discussions

Open Access

EGU

Steiner, J. F., Kraaijenbrink, P. D. A., and Immerzeel, W. W.: Distributed Melt on a Debris-Covered Glacier: Field Observations and Melt Modeling on the Lirung Glacier in the Himalaya, Front. Earth Sci., 0, https://doi.org/10.3389/feart.2021.678375, 2021.

810   Stigter, E. E., Litt, M., Steiner, J. F., Bonekamp, P. N. J., Shea, J. M., Bierkens, M. F. P., and Immerzeel, W. W.: The Importance of Snow Sublimation on a Himalayan Glacier, Front. Earth Sci., 6, 108, https://doi.org/10.3389/feart.2018.00108, 2018.

Stigter, E. E., Steiner, J. F., Koch, I., Saloranta, T. M., Kirkham, J. D., and Immerzeel, W. W.: Energy and mass balance dynamics of the seasonal snowpack at two high-altitude sites in the Himalaya, Cold Regions Science and Technology,

815   183, 103233, https://doi.org/10.1016/j.coldregions.2021.103233, 2021.

Thibert, E., Sielenou, P. D., Vionnet, V., Eckert, N., and Vincent, C.: Causes of Glacier Melt Extremes in the Alps Since 1949, 45, 817–825, https://doi.org/10.1002/2017GL076333, 2018.

Van den Broeke, M. V. D., Reijmer, C., As, D. V., Wal, R. V. de, and Oerlemans, J.: Seasonal cycles of Antarctic surface energy balance from automatic weather stations, Ann. Glaciol.,41, 131–139,

820   https://doi.org/10.3189/172756405781813168, 2005.

Van den Broeke, M. van den, As, D. van, Reijmer, C., and Wal, R. van de: Assessing and Improving the Quality of Unattended Radiation Observations in Antarctica, Journal of Atmospheric and Oceanic Technology, 21, 1417–1431, https://doi.org/10.1175/1520-0426(2004)021<1417:AAITQO>2.0.CO;2, 2004.

Wagnon, P., Ribstein, P., Francou, B., and Pouyaud, B.: Annual cycle of energy balance of Zongo Glacier, Cordillera Real,

825   Bolivia, Journal of Geophysical Research: Atmospheres, 104, 3907–3923, https://doi.org/10.1029/1998JD200011, 1999.

Wagnon, P., Vincent, C., Arnaud, Y., Berthier, E., Vuillermoz, E., Gruber, S., Ménégoz, M., Gilbert, A., Dumont, M., Shea, J. M., Stumm, D., and Pokhrel, B. K.: Seasonal and annual mass balances of Mera and Pokalde glaciers (Nepal Himalaya) since 2007, The Cryosphere, 7, 1769–1786, https://doi.org/10.5194/tc-7-1769-2013, 2013.

830   Wani, J. M., Thayyen, R. J., Ojha, C. S. P., and Gruber, S.: The surface energy balance in a cold and arid permafrost environment, Ladakh, Himalayas, India, The Cryosphere, 15, 2273–2293, https://doi.org/10.5194/tc-15-2273-2021, 2021.

Wolff, M. A., Isaksen, K., Petersen-Øverleir, A., Ødemark, K., Reitan, T., and Brækkan, R.: Derivation of a new continuous adjustment function for correcting wind-induced loss of solid precipitation: results of a Norwegian field study,

835   Hydrology and Earth System Sciences, 19, 951–967, https://doi.org/10.5194/hess-19-951-2015, 2015.

Wu, X., Zhang, W., Li, H., Long, Y., Pan, X., and Shen, Y.: Analysis of seasonal snowmelt contribution using a distributed energy balance model for a river basin in the Altai Mountains of northwestern China, Journal of Hydrology, 35, e14046, https://doi.org/10.1002/hyp.14046, 2021.

Yang, X.: Characteristics of meteorological elements and impact on glacier's change on the north slope of the Mt. Qomolangma
840   Region (Dissertation thesis, p. 125), Cold and Arid Regions Environmental and Engineering Research Institute,
         Chinese Academy of Sciences, 2010.

Yang, W., Guo, X., Yao, T., Yang, K., Zhao, L., Li, S., and Zhu, M.: Summertime surface energy budget and ablation modeling
         in the ablation zone of a maritime Tibetan glacier, Journal of Geophysical Research: Atmospheres, 116,
         https://doi.org/10.1029/2010JD015183, 2011.

845 Zemp, M., Huss, M., Thibert, E., Eckert, N., McNabb, R., Huber, J., Barandun, M., Machguth, H., Nussbaumer, S. U., Gärtner-
         Roer, I., Thomson, L., Paul, F., Maussion, F., Kutuzov, S., and Cogley, J. G.: Global glacier mass changes and their
         contributions to sea-level rise from 1961 to 2016, Nature, 1, https://doi.org/10.1038/s41586-019-1071-0, 2019.

Zhang, G., Kang, S., Fujita, K., Huintjes, E., Xu, J., Yamazaki, T., Haginoya, S., Wei, Y., Scherer, D., Schneider, C., and Yao,
         T.: Energy and mass balance of Zhadang glacier surface, central Tibetan Plateau, J. Glaciol., 59, 137–148,
850   https://doi.org/10.3189/2013JoG12J152, 2013.

Zhu, M., Yao, T., Yang, W., Xu, B., Wu, G., and Wang, X.: Differences in mass balance behavior for three glaciers from
         different climatic regions on the Tibetan Plateau, Clim Dyn, 50, 3457–3484, https://doi.org/10.1007/s00382-017-
         3817-4, 2018.

Zhu, M., Yao, T., Xie, Y., Xu, B., Yang, W., and Yang, S.: Mass balance of Muji Glacier, northeastern Pamir, and its
855   controlling climate factors, Journal of Hydrology, 590, 125447, https://doi.org/10.1016/j.jhydrol.2020.125447, 2020.

Zhu, M., Yang, W., Yao, T., Tian, L., Thompson, L. G., and Zhao, H.: The Influence of Key Climate Variables on Mass
         Balance of Naimona'nyi Glacier on a North-Facing Slope in the Western Himalayas, Geophys Res Atmos, 126,
         https://doi.org/10.1029/2020JD033956, 2021.

Zwaaftink, C. D. G., Mott, R., and Lehning, M.: Seasonal simulation of drifting snow sublimation in Alpine terrain, Water
860   Resources Research, 49, 1581–1590, https://doi.org/10.1002/wrcr.20137, 2013.